Chapter 47

Direction Finding Antennas and Systems

Robert L. Kellogg
Eldon E. Mack
Cathy D. Crews
Argon ST, Fairfax, Virginia

CONTENTS

47.1 INTRODUCTION

Although radio direction finding (DF) is as old as radio itself, new algorithms and new techniques are used in modern digital systems. This chapter looks at the classical underpinnings of DF and its modern applications.

Purpose of Direction Finding

In essence, DF is any technique that determines the direction of a radio transmitter.[1] More formally, radio DF is defined by the National Telecommunications and Information Administration (NTIA) as: "the determination of the position, velocity and/or other characteristics of an object, or the obtaining of information relating to these parameters, by means of the propagation properties of radio waves."[2] Radio DF systems as well as radar and navigation systems are registered in the U.S. Patent system under Class 342.

Application of Direction Finding Systems

The practical applications of DF are numerous:

- **Radio navigation and satellite global positioning services** The terrestrial Long Range Navigation (LORAN) uses phase-comparison of beacon signals for hyperbolic line of bearing (LOB) and geolocation. The U.S. satellite Global Positioning System (GPS) and the Russian counterpart Global Navigation Satellite System (GLONASS) provide time of arrival signals for measuring precise geolocation and velocity.
- **Search and rescue services** The U.S. Coast Guard and worldwide organizations such as COSPAS-SARSAT monitor emergency radio channels for rescue. Both terrestrial and satellite DF networks are used to continuously locate emergency signals.
- **Signal direction finding and location systems** These systems operate throughout the radio spectrum from the high-frequency (HF) band to 18 GHz for purposes that range from animal tracking to locating stolen cars to gathering military intelligence.
- **Homing systems** These are typically small DF systems designed to guide a weapon or artillery shell toward a location. Active RF systems use radar, while passive systems can DF target emitter signals (i.e., "home on jam").
- **Warning systems** Also called Electronic Support Measure (ESM) systems. These are typically rapid response DF and identification systems to protect against hostile radars and homing systems.
- **Radio astronomy** These are characterized by large antenna dishes or arrays that can be synchronized into large interferometric systems spanning continents. The resulting radio maps show density and velocity of natural signals from spin-flip states of hydrogen and various molecular energy state transitions.
- **Smart antennas** Recent advances in adaptive arrays or "smart antennas" provide spatial isolation of emitters, interference cancellation, and resistance to multipath signal fading[3] (see Chapter 25).

Brief History of Direction Finding

Heinrich Hertz began radio DF with experiments in the directionality of antennas in 1888. The first mobile DF system occurred in 1906 when the Stone Radio & Telegraph Co.

installed a direction-indicating device on the U.S. naval collier *Lebanon*. The device was not particularly effective as it "necessitated the swinging of the ship to obtain the maximum signal [strength] and the bearing."[4] In 1915 Dr. Frederick A. Kolster, a former Stone Radio & Telegraph employee working at the U.S. Bureau of Standards, discovered that wire wound on a rectangular frame could be rotated to determine the direction of a signal. One year later, 20 Kolster loop DF systems called the "SE 74" were installed on U.S. ships.[5]

Radio navigation service experiments continued at the U.S. Bureau of Standards, resulting in the first workable aircraft DF system in the early 1920s.[6] The first aircraft DF antennas were manually rotated, but by the 1940s, systems such as the Japanese Type 1-3 system and the Fairchild Aero Compass from which it was copied, provided a twin-loop antenna rotated by a motor.[7]

In the mid-1920s Robert Watson-Watt, inventor of radar, conducted DF research at Ditton Park. Co-researcher Edward Appleton rediscovered the Heavyside propagation layer 300 km above the earth's atmosphere, which Watson-Watt dubbed the "ionosphere".[8] By 1937 the U.S. Navy was using the ionosphere for long-range High Frequency Direction Finding (HFDF, pronounced "Huff-Duff" by old-timers) and in 1941 established both the Atlantic and Mid-Pacific Strategic Direction-Finder Nets, giving Allies the worldwide capability to track German submarines.[9] In 1943 the Germans improved HFDF with the Wullenweber circularly disposed antenna array (CDAA). After the war, it was copied by the Russians (naming their version "Krug") and by the U.S. (whose operators called it the "Elephant Cage" for its size).

The LORAN system was also an outcome of World War II. Developed at the Massachusetts Institute of Technology, the system used a set of continuous wave beacons that could be phase differenced for hyperbolic contours of constant phase. LORAN-C replaced the original LORAN in the 1950s using pulsed signals, resulting in 0.5-km accuracy.

The mathematics for using Doppler direction finding were first developed by the Russian Kotelnikov,[10] but it was the U.S. who launched the first operational satellite system in 1960. The system was called "Transit" and it used a cluster of six low earth orbit (LEO) satellites to provide precise 150/400-MHz reference transmissions.[11] In 1967 the Soviet Union launched Tsyklon, a similar Doppler navigation system.[12] Today the U.S. NAVSTAR GPS and its Russian counterpart, GLONASS, provide precise time, position, and velocity determination worldwide.

Using the same Doppler method as for navigation, Lehan and Brown received U.S. Patent 3063048 for a satellite search and rescue location system.[13] In 1977 the COSPAS-SARSAT satellite search and rescue system was realized as a joint U.S.-Soviet effort that now includes over 35 countries from Algeria to Vietnam.[14]

Since 1980 satellite and terrestrial DF systems have gone through a digital revolution, replacing analog DF processing with digital algorithms such as Bartlett correlation and Schmidt's now famous Multiple Signal Classification (MUSIC) algorithm.[15]

Section 47.2 examines DF systems and sources of error. Section 47.3 looks at specific antenna array systems, while Section 47.4 surveys digital DF algorithms. Section 47.5 explains two techniques for combining LOBs into geolocations, and because of the parallel in approach, Section 47.5 presents a basic Time Difference of Arrival (TDOA) geolocation algorithm.

47.2 DIRECTION FINDING SYSTEM DESIGN

DF systems with antenna arrays determine a signal's LOB by using antenna voltage measurements. While signal direction may be sufficient for many applications, a network of DF systems can combine LOBs to form signal "fixes" or geolocations. Systems that measure time and frequency without antenna arrays may work in a Time Difference of Arrival (TDOA) network to determine signal geolocation directly without LOBs.

System Components

At its core, a DF system requires an antenna array, a receiver to amplify and filter antenna radio frequency (RF) voltages, some means to process the antenna array voltages into a signal angle of arrival (AOA), and an operator display (see Figure 47-1, solid boxes). Modern DF systems now include automated signal detection, classification, digital processing, and remote display (see Figure 47-1, dotted boxes). In all, modern DF systems are comprised of the following elements (numbers correspond to those in Figure 47-1):

1. An antenna or antenna array to collect signal energy from an emitted signal. Arrays can span continents, be compact in a handheld wireless device, or be virtual extensions of an existing array, exploiting techniques such as ESPRIT.[16]
2. An RF distribution system to provide interference filtering, antenna element combining, antenna element selection or switching, and distribution of RF output to the rest of the DF system. An important attribute of the RF distribution system is to allow calibration signals to be switched or multiplexed with the RF input.
3. A calibration system that provides known noise characteristics or test signal amplitude and phase to allow measurement of filter, cable, and receiver effects on system estimates of time, amplitude, and phase.
4. A receiving system to measure the response of the antenna system. RF radio waves are transformed into electron currents. Historic systems used analog measurements and processes to determine DF. Modern systems use analog to digital (A/D) converters to represent signal measurements in digital form.
5. A time and frequency reference system. Modern systems that digitize voltages and use both amplitude and phase information need all receivers and A/D converters synchronized.
6. A DF processor to extract radio determination information such as signal LOB and elevation angle. DF processors may estimate geolocation from multiple signals (e.g., navigation satellites), from coordinated DF systems (e.g. a worldwide HFDF network), or from a single DF system using running LOBs.
7. The DF processor may need extensive antenna array manifold calibration data on the response of the array at different signal angles and different frequencies. Some DF processors, such as the Watson-Watt DF system, use a predetermined mathematical formulation of the signal response. Correlation and eigen decomposition systems process the signal covariance matrix.
8. A signal detection and qualification processor. It is important for the DF processor to provide valid measurement output on signal energy. Further, some systems may qualify the energy as a "signal of interest" before performing DF.
9. In modern DF systems, there is usually a function of signal parameter collection, including time, frequency, angle of arrival, signal strength, etc.
10. If the DF system is on a mobile platform, platform position, velocity, time (PVT), attitude, and heading reference system (AHRS) information is required. This allows transformation of platform measured AOA to earth fixed LOB.
11. Network infrastructure allows control and display to be distributed worldwide to a multitude of users.
12. What was once a simple cockpit indicator has evolved into remote displays of LOBs, emitter location estimates, and confidence error ellipses on a geographical information system (GIS) used by one or many operators.

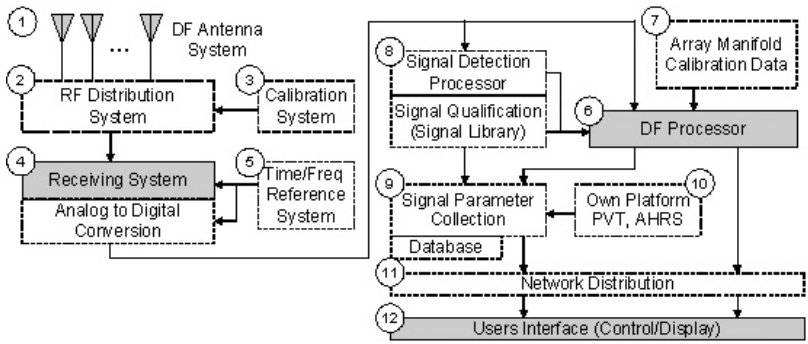

FIGURE 47-1 Traditional (solid boxes) and modern (dotted boxes) DF system design

The use of real-time signal-processing techniques now makes it possible to use phase and amplitude responses, employ antennas of any polarization, and to dynamically calibrate the receiver system for accurate measurements. Now the Internet makes it possible for remote command and control and worldwide data distribution.

System Accuracy and Sources of Error

Direction finding and geolocation system performance are measured primarily in terms of accuracy, timeliness, and throughput. DF accuracy is usually specified in degrees root mean squared (rms), while TDOA systems use rms time. Geolocation accuracy for both is described in terms of a confidence containment ellipse and occasionally in terms of Geometric Dilution of Precision (GDOP). Emitter to receiving site geometry is important and can greatly influence geolocation accuracy. The best geolocation accuracy is obtained when the emitter is in the center of an equilateral triangle of sensor sites.

For DF AOA systems, as a rule of thumb, the array DF accuracy is inversely proportional to the array aperture size. The upper frequency limit of the array is set by the Nyquist spacing of array elements. Ambiguous AOA occurs if the spacing exceeds $c/2f$ where c is the speed of light and f is the highest frequency of operation. DF accuracy degrades proportional to $1/f$ (see Figure 47-2), and there is no distinct bound for lowest frequency of operation. Most common wideband antenna arrays span a frequency range of 1:5 up to 1:8. For example, the VHF/UHF range can be broken into arrays that span 100–500 MHz and 500–3000 MHz.

An array can be made "sparse" when antenna elements are left out of a periodic structure. For example, a simple uniform linear array can be altered to minimal redundancy[17] by leaving certain elements out. Additional elements can be added to an array to provide a larger eigen processing space that gives interference cancellation capability, immunity to fading, and increased hearability, especially in the presence of co-channel signals.

Other key parameters influencing DF accuracy include signal-to-noise ratio (SNR) resulting from a combination of emitter power, propagation distance and path mode (e.g. HF ground wave, ordinary and extraordinary skywave paths, and ionospheric tilting), atmospheric propagation (ducting, especially at VHF and UHF frequencies), atmospheric noise (e.g. lightning in HF), manmade noise (e.g. power line noise, automobile, broadcast

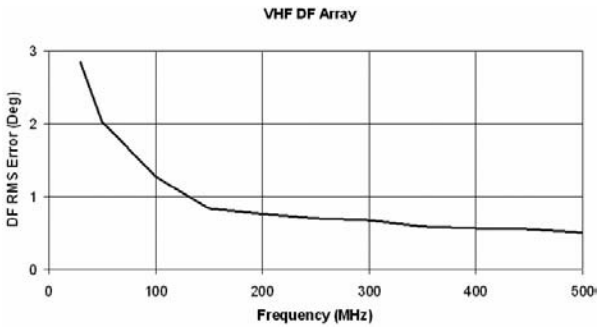

FIGURE 47-2 DF accuracy vs. frequency for VHF array 100–500 MHz

transmitters, etc.), and system internals (antenna gain, cable loss, receiver noise figure, and signal integration time). All of these effects can degrade and possibly corrupt DF results.

Antenna arrays and the systems behind them are usually calibrated and characterized under high SNR conditions, and whenever possible under threshold or minimum SNR conditions. The high SNR conditions establish instrumentation error, while threshold SNR testing more closely predicts operational performance. DF rms error and the Cramer-Rao bound is discussed at the end of Section 47.4.

For TDOA systems, Stein[18] shows that the rms error in measurement from cross correlating two signal samples is based on the Cramer-Rao bound

$$\sigma_{\text{TDOA}} = \frac{\sqrt{3}}{\pi B_s \sqrt{B_{\text{rcv}} T \gamma_{\text{SNR}}}} \tag{47-1}$$

where B_s is the signal bandwidth, B_{rcv} is the receiving system bandwidth, T is correlation time, and γ_{SNR} is the input correlation SNR. γ_{SNR} is derived from the sensor site pair contributing to the correlation

$$\frac{1}{\gamma_{\text{SNR}}} = \frac{1}{2}\left[\frac{1}{\text{SNR}_1} + \frac{1}{\text{SNR}_2} + \frac{1}{\text{SNR}_1 \cdot \text{SNR}_2}\right] \tag{47-2}$$

When the site pair signals are well above the noise floor, the effective γ_{SNR} is just the average of the two intercepts and the cross term $1/\text{SNR}_1\text{SNR}_2$ can be ignored. Under low SNR conditions, all terms must be considered, and under very low SNR conditions, the cross term of Eq. 47-2 dominates. If one of the site pairs has a strong signal intercept, the correlation process can "pull out" the signal from the second site even when the signal is buried in noise (see Table 47-1).[19]

TABLE 47-1 SNR Input, Correlation Gain, and TDOA Measurement Error

Sensor 1 SNR (dB)	Sensor 2 SNR (dB)	Effective Input SNR to Correlator (dB)	Time-Bandwidth Ideal Correlation Gain (dB)	Correlator Peak SNR (dB)	TDOA error (ns)
20	20	20.0	37.0	57.0	16
20	12	14.3	37.0	51.3	30
20	4	6.9	37.0	43.9	71
20	0	2.9	37.0	39.9	111
20	–4	–1.0	37.0	35.9	176

System Calibration and Characterization

A core set of DF processing algorithms relies on the existence of a well-defined array manifold. The array manifold describes the antenna voltage response for an arbitrary N-element array from a set of M signal azimuth angles θ. This can be written in a matrix as

$$\mathbf{a}(\theta) = \begin{bmatrix} a_1(\theta_0) & a_1(\theta_1) & \cdots & a_1(\theta_M) \\ a_2(\theta_0) & a_2(\theta_1) & \cdots & a_2(\theta_M) \\ \vdots & \vdots & \ddots & \vdots \\ a_N(\theta_0) & a_N(\theta_1) & \cdots & a_N(\theta_M) \end{bmatrix} \tag{47-3}$$

Actual array manifolds are composed of more terms than the idealized response to azimuth described in Eq. 47-3. Array manifolds are taken at discrete steps of azimuth over many frequencies (typically at steps ~5 percent of the frequency) and may also include the dimensions of signal elevation and polarization angle. When raw manifold data is measured on a range, the result must be smoothed and interpolated to produce a manifold with uniform azimuth steps. Metadata may be included with the manifold to indicate what frequency, elevation, polarization, or other parameters are used for the manifold creation.

The accuracy of the array manifold typically dominates the system error budget and establishes DF performance. The design of the array can mitigate manifold errors through careful selection of antenna element position and number of elements. Both of these choices are almost always constrained by the platform or site physical boundaries and obstacles, and by the number of processing resources available.

For fixed-site HF antenna arrays, the electrical properties of the ground plane contribute significantly to low angle signal response, particularly the signal magnitude. For this reason, phase-only solutions should be considered. Site errors can be caused by array element interaction with adjacent antennas and nearby structures (mutual coupling, multipath, and blockage), and terrain irregularity (ground plane discontinuities). More information on site errors can be found in Gething.[20]

For transportable or mobile systems, the arrays may need preliminary Numerical Electromagnetics Code (NEC) modeling for antenna position selection. Many times there is a difference between NEC modeling and actual field measurements (see Figure 47-3).

As expected, accurate measurements are typically difficult to obtain near resonant frequencies when the array antennas electrically couple with other antennas or structures. There is an unwritten law of DF that frequency ranges which are difficult to calibrate tend

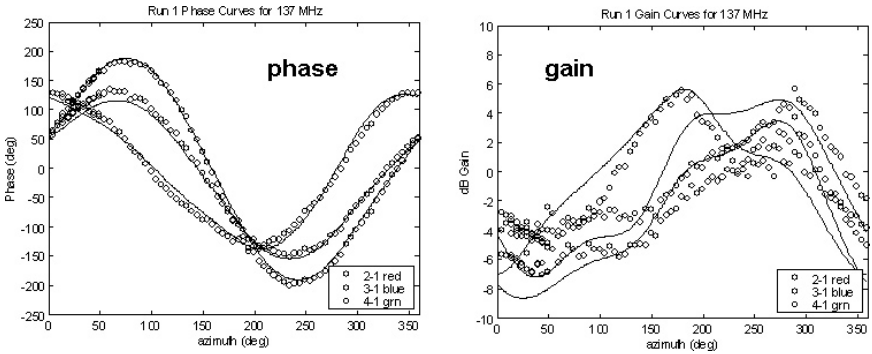

FIGURE 47-3 (*a*) VHF array phase and (*b*) gain comparison between NEC and measurement

to match the ranges where the greatest manifold accuracy is needed. Range calibration planning is required to ensure that all frequencies, azimuth and elevation angles, and signal polarizations are adequately covered.

The process of array manifold generation is performed using "collect" and "verify" functions. For the "collect," test emissions are generated at the frequencies and polarizations of interest and the antenna array is rotated and/or tilted for the range of azimuths and elevations of interest. This may be done at a test range where the antenna array is tilted and rotated, or done on a ship or aircraft moving in a circle, arc, or other pattern at a distance from the test emitter. DF array voltages are recorded in approximately equal steps (e.g. every 1° in azimuth and at FCC allowable frequencies), smoothed, and interpolated to the final array manifold.

For the "verify," the test emitter repeats a subset of the "collect" frequencies and polarizations. Additional frequencies are also included. The DF system receives and processes these emissions using the prepared "collect" array manifolds and computes the LOB rms error to the test emitter. Figure 47-4*a* illustrates LOB error magnitude versus both azimuth (*y*-axis degrees) and frequency (*x*-axis MHz). Figure 47-4*b* plots aggregate rms error (*y*-axis degrees) across the azimuth range versus frequency (*x*-axis MHz). The LOB accuracies expected from the system and array manifold are determined and verified in this fashion.

Built-in system features that facilitate testing of individual antenna elements, cabling loss, time delay and phase error, and overall system processing are vital to long-term AOA direction finding and TDOA geolocation effectiveness. Without such features, degradations in antenna dielectric or temperature changes in electrical properties go uncalibrated. Since DF systems often coexist with other electronic equipment, antenna element responses may change when nearby equipment and structures change. Degradations are manifested as a lack of DF productivity or increase in wild LOB estimates. Antenna designs need to include the ability to inject, couple, and radiate calibration signals without impacting voltage standing wave ratio (VSWR) and reliability.

47.3 DIRECTION FINDING SYSTEM EXAMPLES

This section examines the radio DF systems of the classic Wullenweber CDAA, the popular amateur pseudo-Doppler DF system, the historic Watson-Watt DF system, variations of the *N*-channel DF system, and Butler DF using antenna phase combining.

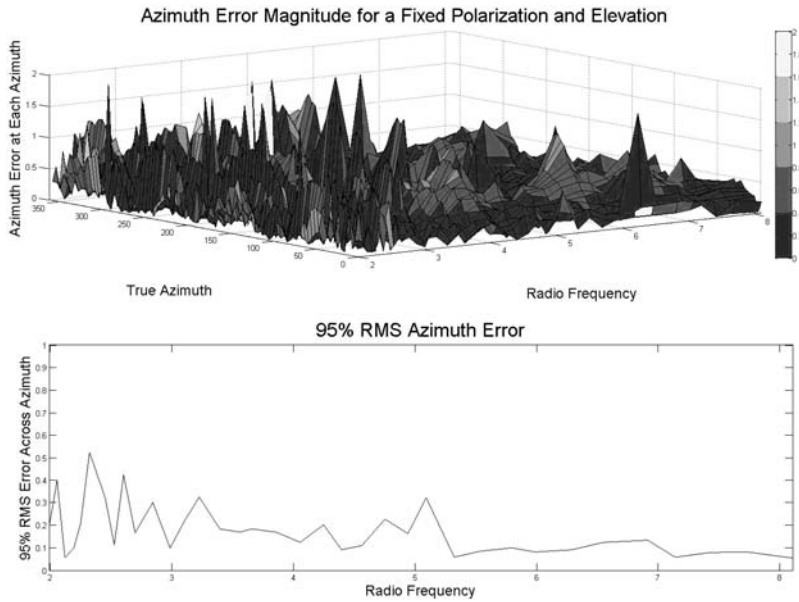

FIGURE 47-4 (*a*) Azimuth error vs. azimuth and frequency and (*b*) mean azimuth error vs. frequency

CDAA Goniometer Direction Finding System

During the 1950s the University of Illinois improved the HFDF Wullenweber CDAA for the U.S. Navy. A ring of 120 monopole antennas was cabled to a central operations building for HF analog beam combining. In the building, matched cables from the antennas were brought together at a circular stator. A spinning rotor, called a *goniometer*, capacitively coupled to 36 contiguous elements of the stator at any moment in time provided both summed and differenced outputs. Thus, the goniometer acted both as a commutator sequentially switching between antenna elements and as a beamformer.

The goniometer delay lines (see Figure 47-5) were electrical lengths equal to the free-space path of the signal to the antenna elements referenced to the center of the goniometer.

The HFDF operator could select either the sum or the difference output on a CRT display with a synchronized rotating time base so that the response pattern of the antenna appeared as a polar beam pattern centered on the direction of the emitter. When searching for an emitter, the sum mode was used, but when the emitter had been identified, the difference mode was used so that the sharp null response pattern displayed azimuth angle with maximum accuracy.

Pseudo-Doppler Direction Finding System

The pseudo-Doppler DF system is a phase-measurement system that uses commutation and stems from the research of Earp and Godfrey in 1947.[21] This DF system is sometimes described in terms of a rotating antenna and the Doppler effect. However, the antennas do not move and there is no change of frequency due to true Doppler ($\Delta f = vf/c$). Rather, this is a clever system that measures signal phase changes using commutated (switched) sequential elements located on the circumference of a circle.

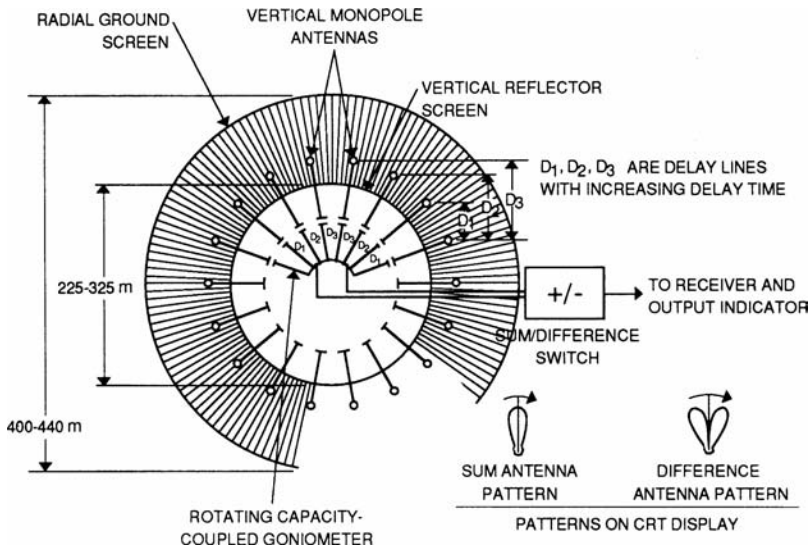

FIGURE 47-5 CDAA array goniometer beamforming

As each antenna element is sampled, the signal phase appears spatially shifted. The pseudo-Doppler DF system (see Figure 47-6) relies on a very short sampling time from each element. This is done by using a simple pin-diode set of switches that funnels each antenna element sequentially into a common RF path. The spatially induced phase shifts become manifest in the FM demodulator as slightly different audio tones. The audio is

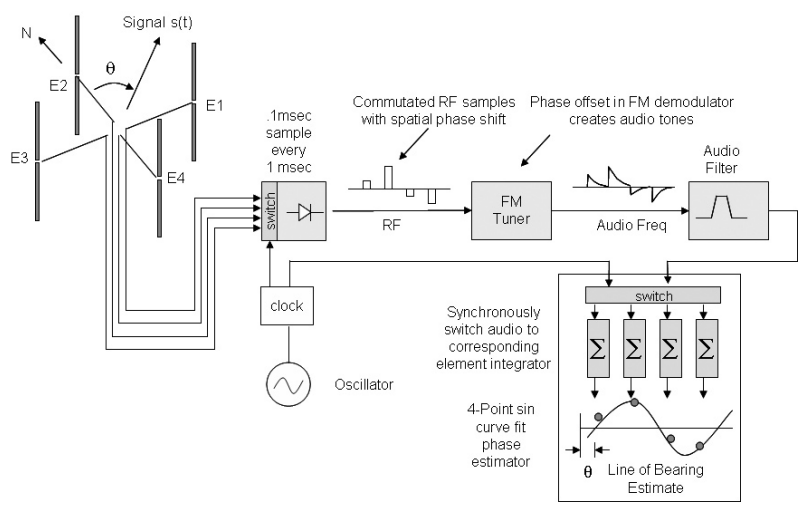

FIGURE 47-6 Pseudo-Doppler DF system using phase commutation

integrated into different summing units, commutating them synchronously at the same clocking speed that sampled the antenna elements. The integrated voltages are fitted with a sine curve whose phase is directly proportional to signal azimuth θ.

Watson-Watt Direction Finding System

The Watson-Watt DF system is a simple, but continuous, amplitude comparison scheme using two orthogonal Adcock beamforming arrays.[22] Each Adcock array is made of two dipole elements that are phase-reversed to create a figure "8" beam pattern (see Figure 47-7). The optimal array spacing is about $\lambda/8$ with relatively short (0.1 λ) dipole element lengths.

The Watson-Watt Adcock DF process (see Figure 47-8) uses two orthogonal Adcock arrays nicknamed the "sine" and "cosine" receiver channels, where the angle of arrival θ is estimated by taking the arctangent of the voltages from these two RF channels.[23]

$$\theta = 90 - \arctan\left(\frac{V_{\sin}}{V_{\cos}}\right) \tag{47-4}$$

The Watson-Watt DF process has two fundamental problems: first, the correct quadrant of the azimuth cannot be determined uniquely, and second, the arctangent approximation deviates as the array diameter to signal wavelength (D/λ) ratio changes. That is, Eq. 47-4 is only an approximation to the true relationship between the two antenna array voltages, which is fully given as

$$\frac{V_{\sin}}{V_{\cos}} = \frac{V(E_2 - E_4)}{V(E_1 - E_3)} = \frac{\sin\left(\frac{\pi D}{\lambda}\sin(\theta)\right)}{\sin\left(\frac{\pi D}{\lambda}\cos(\theta)\right)} \tag{47-5}$$

The LOB error in using the Watson-Watt arctangent approximation is illustrated in Figure 47-9.

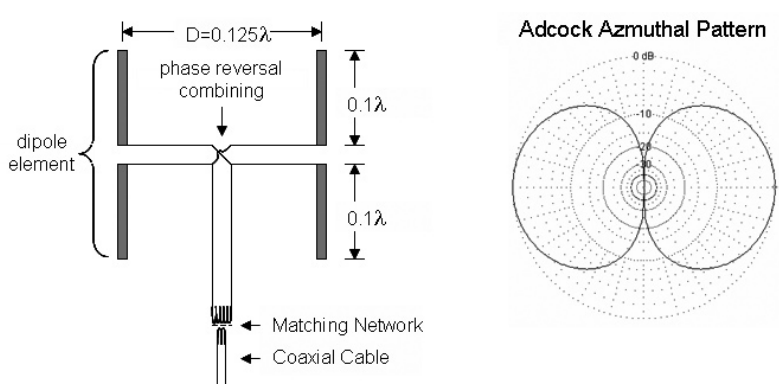

FIGURE 47-7 Adcock antenna and azimuthal beam pattern

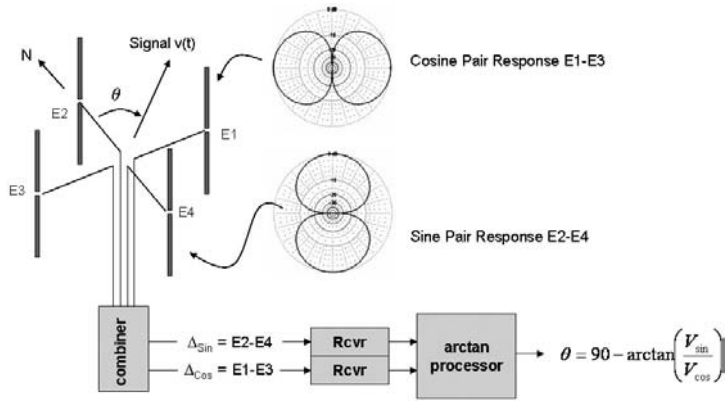

FIGURE 47-8 Watson-Watt DF system

Brueninger Direction Finding System

To correct the deficiencies of Watson-Watt DF, the Brueninger DF system makes a number of improvements:

1. A sense (reference) antenna is used to distinguish signal phase that resolves LOB quadrant ambiguities. The omni antenna may be a separate antenna or can be formed from the sum of all four Adcock elements.

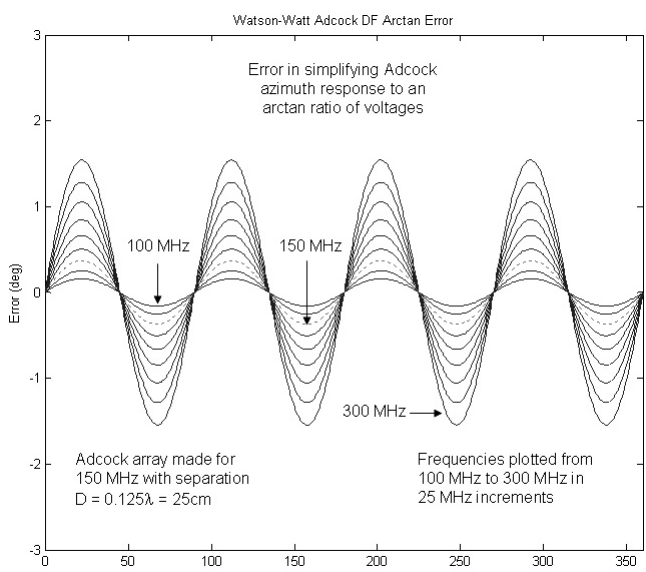

FIGURE 47-9 Watson-Watt DF error

2. More than two antenna elements may be combined to create the sine and cosine beam patterns (e.g. a symmetric set of 8 or 16 dipoles is common).
3. Explicit phase-amplitude correlation methods are used instead of taking the arctangent of voltages (e.g. Bartlett correlation DF is common).

The Brueninger DF uses three RF input channels: omni, sine, and cosine channels. Modern systems use A/D voltage conversion for digital RF processing, as shown in Figure 47-10.

In this example the DF processor implements the Bartlett correlation algorithm exploiting both the phase and amplitude of the voltages. The RF omni, sine, and cosine beam pattern complex voltages (I + jQ, or "IQ" for short) are collected into an array manifold over 0° to 360° in azimuth.

To determine the direction of a signal, the voltages v_o, v_s, and v_c from the omni, sine, and cosine RF channels are measured in K snapshots, forming a voltage matrix representing all data. The voltage matrix is then used to form a time-integrated covariance matrix, **R**:

$$\mathbf{v} = \begin{bmatrix} v_o(1) & v_o(2) & \cdots & v_o(K) \\ v_s(1) & v_s(2) & \cdots & v_s(K) \\ v_c(1) & v_c(2) & \cdots & v_c(K) \end{bmatrix} = \begin{bmatrix} \hat{v}_o \\ \hat{v}_s \\ \hat{v}_c \end{bmatrix} \tag{47-6}$$

where $v_n(k)$ indicates the kth snapshot of complex voltages from element n = omni, sine, and cosine and $\hat{v}_n$ is the time set of voltages with time indices suppressed.

The covariance matrix (Eq. 47-7) is the product of the voltage matrix **v** and its Hermitian transpose $\mathbf{v}^H$ and is normalized by $1/K$ samples:

$$\mathbf{R} = \frac{1}{K}\mathbf{v}\mathbf{v}^H = \frac{1}{K}\begin{bmatrix} \hat{v}_o\hat{v}_o^T & \hat{v}_o\hat{v}_s^T & \hat{v}_o\hat{v}_c^T \\ \hat{v}_s\hat{v}_o^T & \hat{v}_s\hat{v}_s^T & \hat{v}_s\hat{v}_c^T \\ \hat{v}_c\hat{v}_o^T & \hat{v}_c\hat{v}_s^T & \hat{v}_c\hat{v}_c^T \end{bmatrix} \tag{47-7}$$

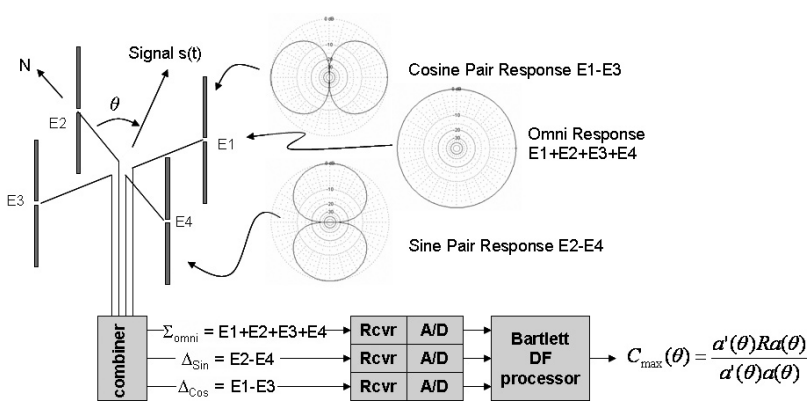

FIGURE 47-10 Brueninger omni, sine, and cosine DF system

Bartlett correlation uses the covariance matrix **R** and the corresponding array manifold $\mathbf{a}(\theta)$ (interpolated to signal frequency) to form a correlation coefficient $C(\theta)$ for every discrete θ in the antenna manifold:

$$C(\theta) = \frac{\mathbf{a}(\theta)^H \mathbf{R}\mathbf{a}(\theta)}{\mathbf{a}(\theta)^H \mathbf{a}(\theta)} \tag{47-8}$$

The coefficient $C(\theta)$ can be normalized to values 0-1 by multiplying by 1/trace(**R**). Once $C(\theta)$ is formed, the Bartlett DF process looks for the maximum $C(\theta)$ using standard peak finding and interpolation techniques (see Figure 47-11*a*). In a simulation, all signal azimuth angles can be examined to create a correlation surface (see Figure 47-11*b*). With a VHF four-element Adcock array 40 cm in diameter, the bearing error at 150 MHz is about 2° rms.

Commutated Direction Finding Systems

As described earlier in this section, the CDAA and pseudo-Doppler DF systems use antenna element commutation. The Brueninger DF system and other arbitrary DF arrays can also be commutated. One antenna element (usually the "omni") is selected as the reference element to which all other antenna elements are sequentially compared. Although the array manifold remains the same, the covariance matrix becomes sparse. For example, if antenna element #1 is the reference element, the covariance matrix for an *N*-element array becomes

$$\mathbf{R} = \frac{1}{K}\begin{bmatrix} \hat{\mathrm{v}}_1\hat{\mathrm{v}}_1^{\mathrm{T}} & \hat{\mathrm{v}}_1\hat{\mathrm{v}}_2^{\mathrm{T}} & \cdots & \hat{\mathrm{v}}_1\hat{\mathrm{v}}_{\mathrm{N}}^{\mathrm{T}} \\ \hat{\mathrm{v}}_2\hat{\mathrm{v}}_1^{\mathrm{T}} & 0 & \cdots & 0 \\ \vdots & \vdots & \ddots & \vdots \\ \hat{\mathrm{v}}_{\mathrm{N}}\hat{\mathrm{v}}_1^{\mathrm{T}} & 0 & \cdots & 0 \end{bmatrix} \tag{47-9}$$

The Bartlett Eq. 47-8 is modified to the commutated form

$$C(\theta) = \frac{\mathbf{R}^H \mathbf{a}(\theta)}{\left[\mathbf{a}(\theta)^H \mathbf{a}(\theta)\right]^{\frac{1}{2}}} \tag{47-10}$$

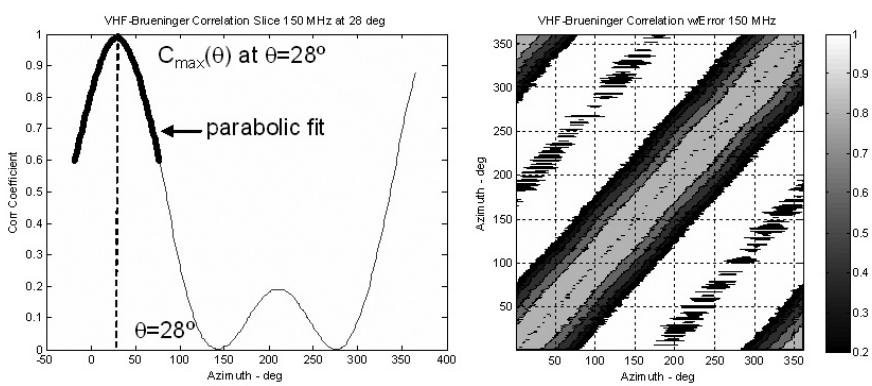

FIGURE 47-11 (*a*) Bartlett correlation with peak finding and (*b*) Bartlett correlation surface

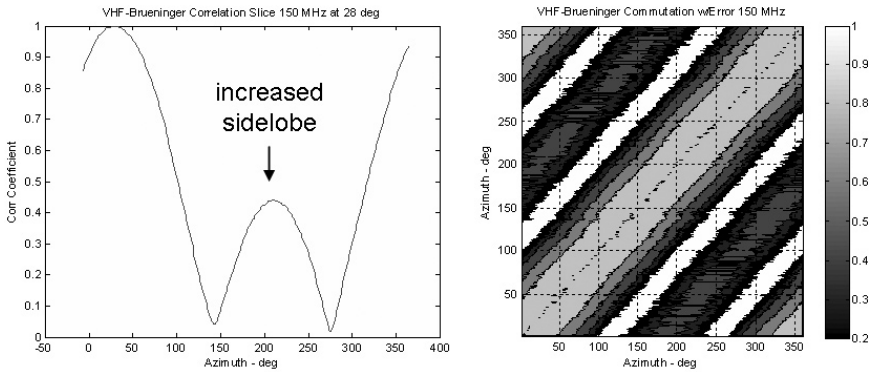

FIGURE 47-12 VHF Brueninger commutated DF (*a*) correlation with signal at 28° and (*b*) correlation surface

In spite of what appears to be a paucity of data, DF commutation using the Bartlett algorithm performs nearly as well as the full *N*-channel solution provided that the total number of voltage samples is the same. However, an *N*-element commutated array takes *N* times longer to collect the same number of RF voltage samples. For example, the Brueninger omni, sine, cosine DF system performing three-channel correlation (see Figure 47-11) can be compared to two different commutation variations: a Brueninger commutated system (see Figure 47-12) and a four-element array that is commutated directly without Adcock element combining (see Figure 47-13). As in the previous section, the array example contains four VHF dipoles on a 40-cm circle operating at 150 MHz. Notice that for Brueninger commutation, there is an increase in spatial sidelobes that is not present in four-element sampling.

Why commutate? Because it reduces the amount of DF hardware by a factor of 2:*N*, which for an 8- or 16-element array can be significant. Regardless of array size, the commutating system only requires two channels of filters, tuners, and A/D converters. Similar efficiencies are gained in digital signal processing. However, the commutation system pays a penalty in time to collect the same number of data snapshots and may totally corrupt the covariance matrix if either the signal transmission is shorter than the commutation cycle time or two or more signals occur at the same frequency during the commutation cycle time.

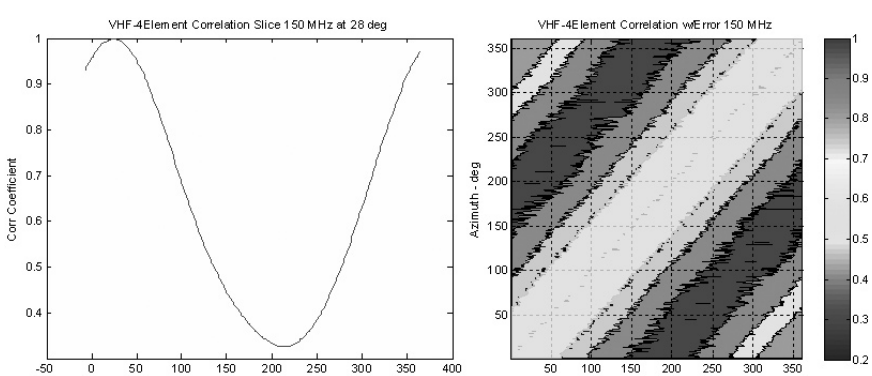

FIGURE 47-13 VHF four-element commutated DF (*a*) correlation with signal at 28° and (*b*) correlation surface

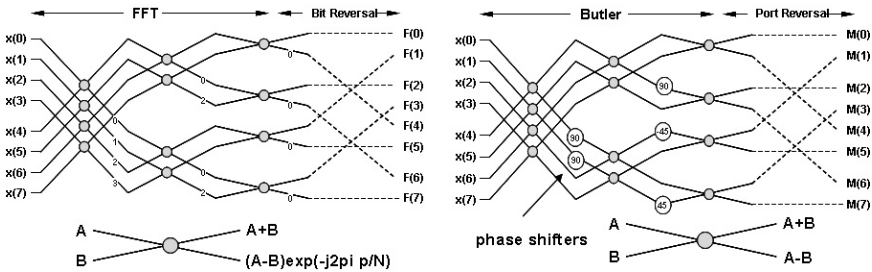

FIGURE 47-14 (*a*) Fast Fourier transform and (*b*) Butler Matrix antenna combining

Butler Direction Finding System

When discussing antenna element combining, people often confuse the Brueninger and Butler combiners. The Brueninger, even in its most complex form, only phase reverses antenna elements by 180° before combining, and the result is always three outputs of an omni, sine, and cosine phased beam pattern. Butler combining, most often implemented as a "Butler Matrix" (see Figure 47-14*b*), is more akin to fast Fourier transform (FFT) and uses combinations of 45°, 90°, and 180° phase shift components.

The FFT example above shows eight inputs and the corresponding eight outputs after "bit reversal" that reorders the output. If the input is time-ordered data, the output is frequency-ordered data with F(0) being the DC component. Butler antenna combining follows the same "butterfly diagram." Each node creates a sum and difference (A + B) and (A – B) without exponential phase weighting. The phase weighting comes at discrete points in the diagram, requiring 45° and 90° phase shifters. If the input is RF energy from eight equally spaced antennas around a circle, the output is spatial phase shifted modes. Mode 0 has no spatial phase shifting with respect to signal azimuth and is exactly equivalent to an omnidirectional beam combiner. Mode 1 and Mode 7 (referred to as Mode –1) have spatial phase shifting proportional to signal azimuth. Similarly Mode 2 and 6 (Mode –2) have spatial phase shifting proportional to twice the signal azimuth. Mode 3 has spatial phase shifting proportional to three times the signal azimuth.

Figure 47-15*a* shows a Monte Carlo simulation of Mode 0 and Mode 1 while Figure 47-15*b* shows the corresponding Butler DF response using the same notional VHF four-element array used earlier in Section 47.3.

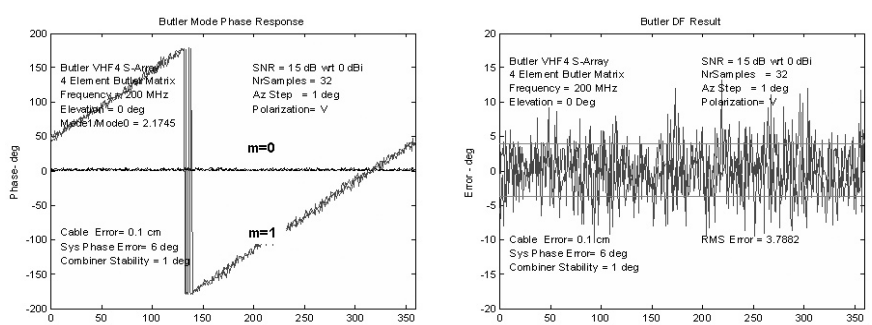

FIGURE 47-15 (*a*) Butler Mode 0 and 1 and (*b*) resulting DF output

The Butler system uses Mode 0 for signal acquisition and reference to which other modes are phase compared. Mode 1 is typically used for coarse DF with the DF algorithm switching to Mode 2 and even Mode 3 for higher resolution. The DF cascade is necessary because Mode 2 and Mode 3 by themselves are double and triple valued over the full azimuth range and need guidance to signal direction from the previous stage.

47.4 DIRECTION FINDING ALGORITHMS

Modern radio DF systems are dependent upon the direction finding algorithm. Section 47.3 introduced the Bartlett DF algorithm, but it is just one of a host of DF solutions. In this section, we consider several classes of DF algorithms, which include correlation-based, eigen-structured, root-finding, and maximum-likelihood algorithms. We then introduce the Cramer-Rao bound (CRB) that specifies the lower bound for DF error due to additive white Gaussian noise. We then compare various DF algorithms against the CRB. Lastly, we consider the effects of correlated cochannel interference on DF performance.

Basic Correlation Algorithms

We have already introduced the Watson-Watt voltage comparison algorithm and Bartlett correlation for Brueninger and commutated arrays. Here we present a comparison of generic DF algorithms that can be applied to any arbitrary array geometry. Two matrices define the environment that the DF algorithms operate in. The first is **a**, the N-element by M-azimuth array manifold that specifies the complex response of each of the N elements over the M azimuths in the field of regard. The second is the sampled signal voltage **v**, which is an $N \times K$ matrix, where K is the number of signal samples:

$$\mathbf{a}(\theta) = \begin{bmatrix} a_1(\theta_0) & a_1(\theta_1) & \cdots & a_1(\theta_M) \\ a_2(\theta_0) & a_2(\theta_1) & \cdots & a_2(\theta_M) \\ \vdots & \vdots & \ddots & \vdots \\ a_N(\theta_0) & a_N(\theta_1) & \cdots & a_N(\theta_M) \end{bmatrix}, \mathbf{v} = \begin{bmatrix} \mathrm{v}_1(0) & \mathrm{v}_1(1) & \cdots & \mathrm{v}_1(K) \\ \mathrm{v}_2(0) & \mathrm{v}_2(1) & \cdots & \mathrm{v}_2(K) \\ \vdots & \vdots & \ddots & \vdots \\ \mathrm{v}_N(0) & \mathbf{v}_N(1) & \cdots & \mathrm{v}_N(K) \end{bmatrix} \quad (47\text{-}11)$$

The covariance matrix remains defined as $\mathbf{R} = \frac{1}{K}\mathbf{v}\mathbf{v}^H$. Using these definitions, various correlation DF algorithms have been created.[24,25]

Bartlett (Normalized):
$$C(\theta) = \left(\frac{1}{tr(\mathbf{R})}\right)\frac{\mathbf{a}(\theta)^H \mathbf{R}\mathbf{a}(\theta)}{\mathbf{a}(\theta)^H \mathbf{a}(\theta)} \quad (47\text{-}12)$$

Capon (Classic):
$$C(\theta) = \frac{\mathbf{a}(\theta)^H \mathbf{a}(\theta)}{\mathbf{a}(\theta)^H \mathbf{R}^{-1}\mathbf{a}(\theta)} \quad (47\text{-}13)$$

Capon (Smooth):
$$C(\theta) = 1 - \frac{\mathbf{a}^H(\theta)\mathbf{R}^{-1}\mathbf{a}(\theta)}{\mathbf{a}^H(\theta)\mathbf{a}(\theta)} \quad (47\text{-}14)$$

Maximum Entropy:
$$C_k(\theta) = \frac{\mathbf{a}(\theta)^H \mathbf{a}(\theta)}{\mathbf{a}(\theta)^H c_k c_k^H \mathbf{a}(\theta)} \quad (47\text{-}15)$$

The performance of these algorithms will be given later in the chapter, in the section "DF Algorithm Comparison." For the Bartlett algorithm, we included the factor 1/trace(**R**) to ensure $C(\theta)$ varies between zero and one. The Capon algorithm is written in both its classic form and in a smooth (inverted) form that ensures $C(\theta)$ varies between zero and one and allows easier peak interpolation when using discrete array manifold θ steps. For the Maximum Entropy algorithm, $\boldsymbol{c_k}$ is the kth column vector of the inverse covariance matrix ($\mathbf{R}^{-1}$).

Eigen Structured Algorithms

Many DF algorithms depend upon decomposing the covariance matrix into subspaces that comprise the signal and noise. One of the first spectral estimation methods using eigenvectors was developed in 1973 by V. F. Pisarenko,[26] whose eigen method originally focused on harmonic decomposition. The Min-Norm eigen approach was developed in 1983 by Kumaresan and Tufts.[27] However, the most popular and versatile algorithm is Schmidt's 1986 MUSIC algorithm.[15] The algorithms are

Pisarenko:
$$C_k(\theta) = \frac{1}{\left|a(\theta)^H \bar{e}_k\right|^2} \tag{47-16}$$

Min-Norm:
$$C_k(\theta) = \frac{\left(u_k^T \mathbf{E}_N \mathbf{E}_N^H u_k\right)^2}{\left|\mathbf{a}(\theta)^H \mathbf{E}_N \mathbf{E}_N^H u_k\right|^2} \tag{47-17}$$

MUSIC (classic):
$$C(\theta) = \frac{1}{\mathbf{a}(\theta)^H \left\{\mathbf{E}_N \mathbf{E}_N^H\right\} \mathbf{a}(\theta)} \tag{47-18}$$

MUSIC (smooth):
$$C(\theta) = 1 - \frac{\mathbf{a}^H(\theta)\left\{\mathbf{E}_N \mathbf{E}_N^H\right\}\mathbf{a}(\theta)}{\mathbf{a}^H(\theta)\mathbf{a}(\theta)} = \frac{\mathbf{a}^H(\theta)\left\{\mathbf{E}_S \mathbf{E}_S^H\right\}\mathbf{a}(\theta)}{\mathbf{a}^H(\theta)\mathbf{a}(\theta)} \tag{47-19}$$

The performance of these algorithms will also be given later in the chapter, in the section "DF Algorithm Comparison." For the Pisarenko algorithm, $\bar{e}_k$ is one or more eigenvectors associated with the smallest (noise) eigenvalues. The span of the eigenvectors is of dimension N, the number of elements in the array. We normally expect only one signal present for DF. Hence the signal eigenvector $\mathbf{E}_S$ is of dimension $N \times 1$, and $\mathbf{E}_N$, the matrix of noise eigenvectors, is of dimension $N \times (N-1)$. If D co-channel signals are present in the voltage samples that make up the covariance matrix, $\mathbf{E}_S$ is an $N \times D$ subspace and $\mathbf{E}_N$ is an $N \times (N-D)$ subspace.

For the Min-Norm algorithm, $\boldsymbol{u_k}$ is the kth column of an $N \times N$ identity matrix. The MUSIC algorithm is presented in its classical form in Eq. 47-18, which shows distinctive sharp spectral peaks, and is presented in a smoothed form in Eq. 47-19, which has smoother peaks and is easier to interpolate when using a discrete array manifold. Further, MUSIC is written using either the noise or signal eigenvectors $\mathbf{E}_N$ or $\mathbf{E}_S$: choose the form that has the smaller subspace for the lowest computational load.

Root DF Algorithms

Root DF algorithms are specialty DF algorithms applicable to only uniformly spaced linear arrays with N elements, where the array manifold can be written using an index to specify the array element of interest. The array manifold is then written as

$$\mathbf{a}(\theta, n) = \exp\left(-jn\frac{2\pi d}{\lambda}\cos(\theta)\right) \tag{47-20}$$

where n goes from $-(N-1)/2$ to $(N-1)/2$ (odd-numbered element arrays), λ is the signal wavelength, and d is the spacing between elements. For a standard linear array, just at the Nyquist limit, $d = \lambda/2$. Then Eq. 47-20 reduces to

$$\mathbf{a}(\theta, n) = \exp(-jn\pi\cos(\theta)) \tag{47-21}$$

The array manifold can further be transformed into a vector of polynomial coefficients z by using the representation

$$z = \exp(j\pi\cos(\theta)) \quad \text{giving} \quad \mathbf{a}_z(z) = [1 \quad z \quad \cdots \quad z^{N-1}]^T \tag{47-22}$$

The most common DF approach is the Root MUSIC algorithm using noise subspace eigenvectors. The correlation coefficient is written in terms of the eigenvector noise subspace and the antenna manifold as

$$C(z) = \mathbf{a}^T\left(\frac{1}{z}\right)\{\mathbf{E}_N\mathbf{E}_N^H\}\mathbf{a}(z) \tag{47-23}$$

The Root MUSIC algorithm computes the roots of $C(z)$ and chooses the D roots, $\hat{z}_i$, that lie inside a unit circle and are closest to the unit circle. The estimates of signal azimuth $\hat{\theta}_i$ are found by the inverse relation between θ and z for the $i = 1 \ldots D$ roots, giving

$$\hat{\theta}_i = \cos^{-1}\left(\frac{\arg(\hat{z}_i)}{\pi}\right) \tag{47-24}$$

From Eq. 47-24 it can be seen that Root MUSIC is not affected by the magnitude of $\hat{z}_i$. Thus we expect Root MUSIC to provide a better estimate of signal direction than the classical MUSIC algorithm. The performance of these algorithms is given later in the chapter, in the section "DF Algorithm Comparison."

Since the Min-Norm algorithm also uses eigenvectors of the noise subspace, we expect that there should be a Root Min-Norm algorithm that is a better estimator than Eq. 47-17. While the development of both root MUSIC and Root Min-Norm is developed using a uniformly spaced linear array, these algorithms are applicable to circular arrays as well. The starting point for Root Min-Norm begins by defining a subspace vector $\mathbf{d}$, of dimension $N \times 1$, that has the property of being orthogonal to the signal subspace. That is, given the array manifold $\mathbf{a}(\theta_i)$ at discrete θ_i for $i = 1 \ldots D$ signal directions, $\mathbf{d}$ has the property

$$\mathbf{a}(\theta_i)^H\mathbf{d} = 0 \tag{47-25}$$

The only set of vectors orthogonal to the signal vectors is the set of noise eigenvectors with arbitrary magnitude. Thus the vector $\mathbf{d}$ is found as a weighted noise subspace eigenvector

$$\mathbf{d} = w^{\frac{1}{2}}\mathbf{E}_N = \left(\frac{\mathbf{c}^*}{\mathbf{c}^H\mathbf{c}}\right)\mathbf{E}_N \tag{47-26}$$

where **c** is created from the first elements of each of the noise eigenvectors. As with Root MUSIC, Root Min-Norm uses the transform $z_i = \exp(j\pi \cos(\theta_i))$ to represent the $i = 1...D$ signal directions, allowing **d** to be written in polynomial form

$$D(z) = 1 + d_1 z^{-1} + ... + d_N z^{-N} \tag{47-27}$$

The polynomial roots of $D(z)$ provide the estimate of $\hat{z}_i$, which are selected within and close to the unit circle. The inverse trigonometric transform of Eq. 47-24 converts $\hat{z}_i$ to the Root Min-Norm estimate of signal arrival $\hat{\theta}_i$ for the $i = 1 \ldots D$ signals.

Maximum Likelihood DF Algorithms

The Maximum Likelihood (ML) estimator for the direction $\hat{\theta}_i$, for $i = 1...D$ signals, uses a signal subspace that is as close as possible to the data subspace. This is formulated by taking the maximum of

$$\theta_{\text{ml}} = \arg\max_{\theta} \{tr[\mathbf{P}_\theta \mathbf{R}]\} \tag{47-28}$$

where **R** is the covariance matrix of the antenna array voltage data and $\mathbf{P}_\theta$ is the projection vector of the $i = 1...D$ signals. $\mathbf{P}_\theta$ is formed from the discrete $N \times D$ steering vectors $\mathbf{a}(\theta_i)$ as

$$\mathbf{P}_\theta = \mathbf{a}(\theta_i)\left(\mathbf{a}(\theta_i)^H \mathbf{a}(\theta_i)\right)^{-1} \mathbf{a}(\theta_i)^H \tag{47-29}$$

To search over the actual N-elements by the M-azimuth array manifold $\mathbf{a}(\theta)$, the computational complexity of the ML algorithm is $O(M^D)$. Fortunately there is a way to reduce computational complexity to find $\mathbf{P}_\theta$. The alternating projection maximization (APM) algorithm, invented by Ziskind and Wax,[28] replaces the multidimensional maximization problem with a sequence of one-dimensional maximization problems, reducing the computational complexity to $O(MD)$.

The first step of the APM algorithm is an initialization step where θ_i^0 is estimated for $i = 1...D$ signals. θ_1^0 is estimated by finding the angle θ that maximizes Eq. 47-28 assuming only one signal is present. θ_2^0 is found by assuming the first signal is at θ_1^0 and maximizing Eq. 47-28 for the second signal. The initialization is complete after repeating for D signals.

Next, a projection of the manifold is created so that all of the manifold vectors are orthogonal to all of the estimated steering vectors except the steering vector that is being updated. Notationally, $\mathbf{a}(\hat{\theta}_i)$ represents the set of steering vectors for all of the estimated signals except for signal i. APM creates a projected manifold **b** such that the vector at each θ, $\mathbf{b}(\theta, \hat{\theta}_i)$ is orthogonal to all of the vectors in $\mathbf{a}(\hat{\theta}_i)$. That is

$$\mathbf{b}(\theta, \hat{\theta}_i)\mathbf{a}(\hat{\theta}_i) = \mathbf{0} \tag{47-30}$$

APM then determines θ_i^{k+1} for iteration $k + 1$ and signal i as

$$\theta_i^{k+1} = \arg\max_{\theta_i} \mathbf{b}\left(\theta, \hat{\theta}_i^k\right)^H \mathbf{R}\mathbf{b}\left(\theta, \hat{\theta}_i^k\right) \tag{47-31}$$

The iterations are repeated until a criterion δ is reached such that

$$\left|\theta_i^{k+1} - \theta_i^k\right| < \delta \tag{47-32}$$

Power Method Algorithms for Eigen Structures

In this section we investigate ways of computing eigenvalues and eigenvectors efficiently. Many computer languages provide a Linear Algebra extension from the LAPACK library to compute eigenvectors and eigenvalues quickly.[29] For an N-element array, this requires $O(N^3)$ operations. For many applications, the LAPACK library meets all computational needs. Although efficient, the standard LAPACK library has a highly complex logical structure that cannot be implemented efficiently in pipeline hardware such as Field Programmable Gate Arrays (FPGAs).

The Jacobi algorithm for computing eigenvalues and eigenvectors is not optimal in terms of multiply, divide, and add operations, but it can be implemented using Coordinate Rotation Digital Computer (CORDIC) processes[30] that are suitable for pipeline hardware. Ahmedsaid et al[31] implemented the Jacobi algorithm using CORDIC blocks for an 8×8 covariance matrix. Computing the eigenvectors and values to 14-bit resolution required 16,681 slices and approximately 18,000 clock cycles.

Another pipeline approach is the "power method" by Stewart,[32] which shows there is an extremely simple way of estimating the dominant eigenvector, $\mathbf{E}_1$, from a covariance matrix $\mathbf{R}$:

$$\mathbf{E}_1 = \mathbf{R}^k\mathbf{R}(m) = (\mathbf{L}\mathbf{L}^H)^k\mathbf{L}\mathbf{L}(m)^H \tag{47-33}$$

where k is an integer > 0, $\mathbf{R} = \mathbf{L}\mathbf{L}^H$, $\mathbf{R}(m)$ is a column vector from $\mathbf{R}$, and $\mathbf{L}(m)$ is a row vector from $\mathbf{L}$. In the case of a single signal with positive SNR, $\mathbf{E}_1$ (an orthonormal vector) can be used in place of $\mathbf{E}_s$ in the MUSIC DF of Eq. 47-19 and is quickly solved.

With a modest extension, the power method is able to determine a set of orthonormal vectors and bases to replace the eigenvectors and values of multiple signals. Once $\mathbf{E}_1$ has been found, the $\mathbf{L}$ matrix is updated as

$$\mathbf{u} = \mathbf{E}_n^H\mathbf{L}_n \tag{47-34}$$

$$\mathbf{L}_{n+1} = \mathbf{L}_n - \mathbf{E}_n\mathbf{u} \tag{47-35}$$

where $\mathbf{E}_n$ is normalized such that $\mathbf{E}_n^H\mathbf{E}_n = 1$. The corresponding basis value λ_n is then estimated as

$$\lambda_n = \mathbf{u}^H\mathbf{u} \tag{47-36}$$

This procedure is repeated to estimate $\mathbf{E}_n$ and λ_n from $n = 1$ to N array elements. In all, the power method requires $(2k + 4)N^3 - (2k + 1)N^2 - 2N$ multiply and accumulate (MAC) operations. Up to $N = 8$ and $k = 2$ MAC operations can be supported using modern FPGAs.

Cramer-Rao DF Error Limit

Before evaluating each of the algorithms given in the preceding section, we would like a baseline that gives the limit of DF performance for any given array and incoming co-channel set

of signals. This can be obtained using the Cramer-Rao bound (CRB) where additive white Gaussian noise (AWGN) corrupts the received signal voltages without bias. A thorough treatment is given by Van Trees.[33]

We start with a model of the received signal $\mathbf{V}$ as an $M \times K$ matrix of voltages sampled at each of M antenna array elements over K snapshots. (We use M vice N to avoid confusion with the noise component $\mathbf{N}$.) $\mathbf{V}$ is the result of D co-channel signals $\mathbf{S}$ received through the array manifold $\mathbf{a}(\theta)$ plus direction independent noise $\mathbf{N}$. $\mathbf{S}$ is a $D \times K$ matrix, while $\mathbf{N}$ is an $M \times K$ diagonal matrix of AWGN noise samples with variance σ_w^2.

$$\mathbf{V} = \mathbf{a}(\theta)\mathbf{S} + \mathbf{N} \tag{47-37}$$

Using this separation of signal and noise, the covariance matrix $\mathbf{R}_V$ of measured voltages can be written in terms of signal and noise as well:

$$\mathbf{R}_V = \mathbf{R}_S + \mathbf{R}_N = \mathbf{a}(\theta)\mathbf{S}_f\mathbf{a}(\theta)^H + \sigma_w^2\mathbf{I} \tag{47-38}$$

where $\mathbf{R}_S$ is the signal covariance matrix (equal to $\mathbf{a}(\theta)\mathbf{S}_f\mathbf{a}(\theta)^H$), $\mathbf{R}_N$ is the noise covariance matrix (equal to $\sigma_w^2\mathbf{I}$), and $\mathbf{S}_f$ is the $D \times D$ signal matrix (equal to $\mathbf{SS}^H$). The resulting Cramer-Rao bound of variance becomes

$$\mathbf{C}_{\mathrm{CR}}(\theta) = \frac{\sigma_w^2}{2K}\left\{\mathrm{Re}\left[\left[\frac{\partial \mathbf{a}(\theta)^H}{\partial\theta}\mathbf{P}_\theta^\perp\frac{\partial \mathbf{a}(\theta)}{\partial\theta}\right]\circ\left[\mathbf{S}_f\mathbf{a}(\theta)^H\mathbf{R}^{-1}\mathbf{a}(\theta)\mathbf{S}_f\right]^T\right]\right\}^{-1} \tag{47-39}$$

where $\circ$ is the Hadamard product of two matrices using element by element multiplication and $\mathbf{P}_\theta^\perp$ is the projection matrix of the array manifold onto the noise subspace and is defined as

$$\mathbf{P}_\theta^\perp = \mathbf{I} - \mathbf{a}(\theta)(\mathbf{a}(\theta)^H\mathbf{a}(\theta))^{-1}\mathbf{a}(\theta)^H \tag{47-40}$$

Clearly the CRB decreases with increasing data samples, K, and decreasing noise variance. At high SNR the CRB is proportional to σ_w^2, but at low SNR, the CRB is proportional to σ_w^4. The transition from low to high SNR is determined by the signal correlation, spatial separation of the signals, and the beamwidth of the array. As the signals become more correlated, $\mathbf{R}_S$ becomes less diagonal, increasing the CRB. As the separation of the signal steering vectors $\mathbf{a}(\theta)^H\mathbf{a}(\theta)$ becomes less diagonal, CRB likewise increases.

DF Algorithm Comparison

Monte Carlo simulations were run to compare DF performance in which two uncorrelated, equal power signals impinge on a standard linear array with elements spaced $\lambda/2$ apart. The signals were positioned nearly broadside to the array at azimuths of 87.5° and 92.5°. The array SNR (ASNR) was varied from –20 dB to +30 dB and resulting DF rms errors were determined from 200 trials per algorithm. Each trial uses 100 data (voltage) snapshots with additive white Gaussian noise.

If only one signal is present in the array manifold (per frequency channel, etc.), all computational methods produce the same directional estimate, with Bartlett correlation the simplest to implement. The Bartlett correlation algorithm can be used on many different array geometries, can handle Brueninger element combining, and can be used in commutating systems. But the Bartlett DF algorithm cannot resolve closely spaced co-channel

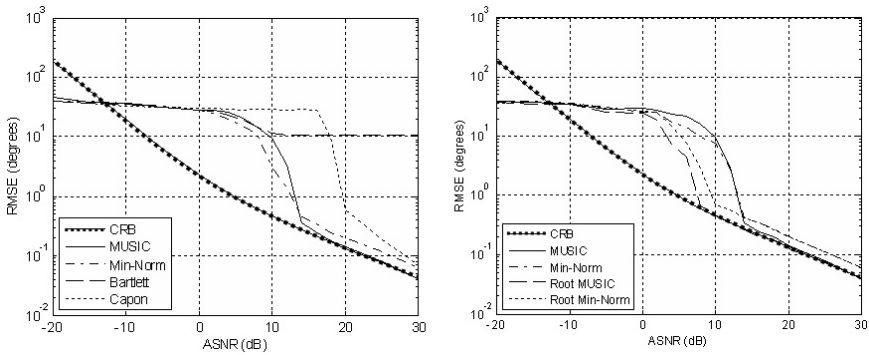

FIGURE 47-16 (*a*) Basic DF and Eigen algorithm DF performance and (*b*) Eigen and Root algorithm DF performance

signals. The Capon method provides much better signal resolution than Bartlett, but eigen structure methods provide even more capability. The Min-Norm algorithm provides slightly better performance than MUSIC at low ASNR, but with much more complexity (see Figure 47-16*a*). For restricted array geometry, Root MUSIC and Root Min-Norm give better DF performance than their general array counterparts MUSIC and Min-Norm. Root MUSIC is slightly better than Root Min-Norm in accuracy and is considerably more efficient to compute (see Figure 47-16*b*).

The power method creating orthogonal basis vectors and values can be used in the MUSIC, Root MUSIC, Min-Norm, and Root Min-Norm algorithms just as the eigenvectors and values are used. In a DF simulation consistent with the other comparisons in this section, the eigen decomposition required double floating point values (64 bits) while the power method used only 18-bit integer multipliers and 48-bit integer accumulators. The power method thus provides significant computational load savings without loss of accuracy (see Figure 47-17).

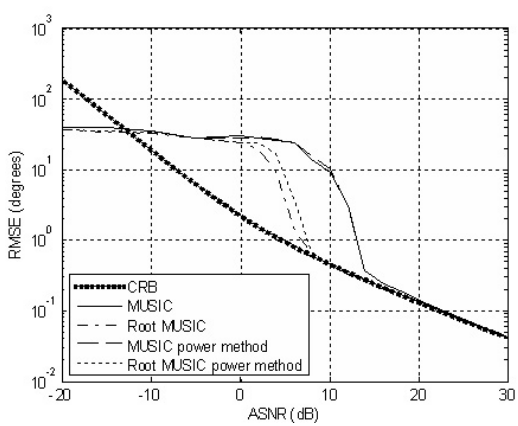

FIGURE 47-17 DF performance of Eigen versus power method implementations

Estimating the Number of Co-Channel Signals

For an N-element array, eigen decomposition of the covariance matrix gives N eigenvalues λ and corresponding eigenvectors $\mathbf{E}$. The eigen subspace is divided into $\mathbf{E}_S$, a subspace of $1 \ldots D$ signal eigenvectors, and $\mathbf{E}_N$, a subspace of $(N - D)$ noise vectors. These eigenvectors and their eigenvalues are related to the original covariance matrix as

$$\mathbf{R} = \mathbf{E}_S \lambda_S \mathbf{E}_S^H + \mathbf{E}_N \lambda_N \mathbf{E}_N^H \tag{47-41}$$

The problem is to estimate the number of signals D when the noise eigenvalues λ_N can be represented by a span of $(N - D)$ noise terms containing AGWN,

$$\lambda_N = \text{diag}\left[\sigma_w^2 \ldots \sigma_w^2\right] \tag{47-42}$$

An ad hoc ratio test can be established to compare the smallest eigenvalue with the $(N - 1)$ remaining eigenvalues in a threshold test. An optimal approach uses the likelihood ratio that challenges the hypothesis that the $(N - D)$ smallest eigenvalues are equal against the hypothesis that the $(N - D - 1)$ smallest eigenvalues are equal. Van Trees[34] shows that for a covariance matrix $\mathbf{R}$, created from K snapshots and decomposed into N eigenvalues, the likelihood of D signals, $L(D)$, can be written as

$$L(D) = K(N - D) \ln \left\{ \frac{\dfrac{1}{N - D} \displaystyle\sum_{i=D+1}^{N} \lambda_i}{\left(\displaystyle\prod_{i=D+1}^{N} \lambda_i \right)^{\frac{1}{N-D}}} \right\} \tag{47-43}$$

The term in the brackets is the ratio of the arithmetic mean of the $(N - D)$ smallest eigenvalues to the geometric mean of $(N - D - 1)$ eigenvalues. If the $(N - D)$ smallest eigenvalues are equal (i.e., have the same noise variance σ_w^2) then the arithmetic and geometric means are equal and $L(D) = 0$.

Two common tests use this likelihood ratio to determine the number of signals present: the Akaike information-theoretic criterion (AIC)[35] and the minimum description length (MDL) of Wax and Kailath.[36] These tests add a penalty function based on the degrees of freedom of the likelihood function. Akaike introduces AIC as

$$D_{\text{AIC}} = \arg\min_D \{L\ (D) + [D(2N - D)]\} \tag{47-44}$$

while the MDL test uses

$$D_{\text{MDL}} = \arg\min_D \left\{ L(D) + \frac{1}{2}[D(2N - D) + 1] \ln K \right\} \tag{47-45}$$

As with any eigen structure method, the power method of determining orthonormal vectors and values may be substituted. For the antenna array and simulation parameters defined in the preceding section, the AIC test (using eigen structures or orthonormal vectors) has a better probability of signal detection at low ASNR than the MDL test. Both AIC and MDL may underestimate the number of signals present. Above 8 dB, all methods successfully estimate the presence of two signals (see Figure 47-18).

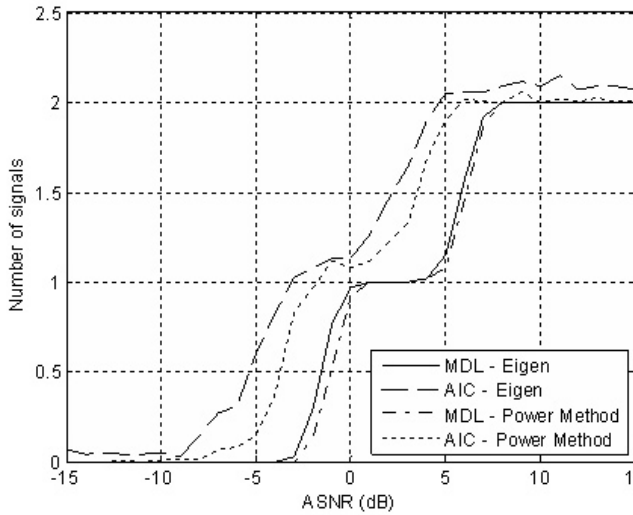

FIGURE 47-18 Estimates of the number of signals present vs. array signal-to-noise ratio (ASNR)

DF when Co-Channel Signals Are Correlated

All of the DF algorithms discussed so far have some ability to separate co-channel signals. But none can separate perfectly correlated or coherent signals. They cannot separate the signals because the signal covariance matrix, $\mathbf{S}_f$ as defined in Eq. 47-38, has a rank of one for coherent signals.

Unfortunately, multiple signal correlation generally occurs in a multipath situation. That is, a single signal travels on multiple paths from the transmitter to the receiving antenna array. If the signal arrives on two paths that are equal length, then the antenna array would see two signals that are 100 percent correlated. As the path length difference increases, the correlation ratio drops. An estimate of the correlation, ρ, is given

$$\rho = 1 - \frac{B \cdot \Delta\text{path}}{c} \tag{47-46}$$

where B is signal bandwidth, $\Delta path$ is the path length difference, and c is the velocity of light. For example, if the signal bandwidth is 25 kHz and the path length difference is 600 meters, then $\rho = 0.95$.

A Monte Carlo simulation similar to that used previously in Section 47.4 was used to evaluate MUSIC and Root MUSIC using two signals with 95 percent correlation (see Figure 47-19). At low ASNR, both MUSIC and Root MUSIC are erroneous, randomly determining the DF. Even a moderately strong ASNR of 10–12 dB still produces random DF. Only when the SNR is greater than 15 dB does Root MUSIC begin to determine the correct direction of both signals, while the classic MUSIC algorithm needs ASNR > 25 dB to produce useful DF. Both Root MUSIC and classic MUSIC can resolve highly correlated, closely spaced signals given sufficient ASNR.

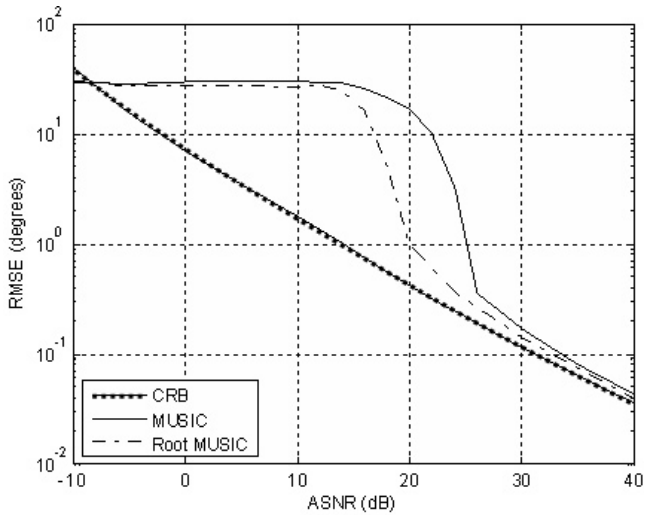

FIGURE 47-19 DF performance for two closely spaced signals that are 95 percent correlated

47.5 GEOLOCATION ALGORITHMS

In this section, we present three geolocation algorithms. The Stansfield algorithm is the oldest and has been used successfully in both worldwide HFDF systems and line-of-sight angle-of-arrival systems as well. The Wangsness algorithm uses LOBs drawn on a spherical earth and likewise can be used globally or locally for geolocation solutions. A simple 2D TDOA geolocation algorithm is also presented. These three approaches are compared using confidence ellipse containment.

Stansfield AOA Geolocation Algorithm

The Stansfield algorithm[37] was developed during World War II for AOA geolocation using a flat (Cartesian) geometry, illustrated in Figure 47-20.

The LOB from a receiving site has a bearing angle β from north (y-axis). Using an arbitrary coordinate system, the LOB is also described by d, the perpendicular distance to the coordinate system origin; m is the LOB miss distance from point $(p_x, p_y)^T$.

The miss distances from a set of K lines of bearing with common Cartesian origin created by some number of DF sites is written in matrix form as

$$\mathbf{m} = \mathbf{A}\mathbf{p} + \mathbf{d} \tag{47-47}$$

where $\mathbf{m}$ is the miss vector, $\mathbf{A}$ is a transformation matrix, $\mathbf{p}$ is the position vector, and $\mathbf{d}$ is the LOB origin offset parameter:

$$\mathbf{m} = \begin{bmatrix} m_1 \\ m_2 \\ \vdots \\ m_K \end{bmatrix}, \mathbf{A} = \begin{bmatrix} -\cos(\beta_1) & \sin(\beta_1) \\ -\cos(\beta_2) & \sin(\beta_2) \\ \vdots & \vdots \\ -\cos(\beta_K) & \sin(\beta_K) \end{bmatrix}, \mathbf{p} = \begin{bmatrix} p_x \\ p_y \end{bmatrix}, \text{and } \mathbf{d} = \begin{bmatrix} d_1 \\ d_2 \\ \vdots \\ d_K \end{bmatrix}$$

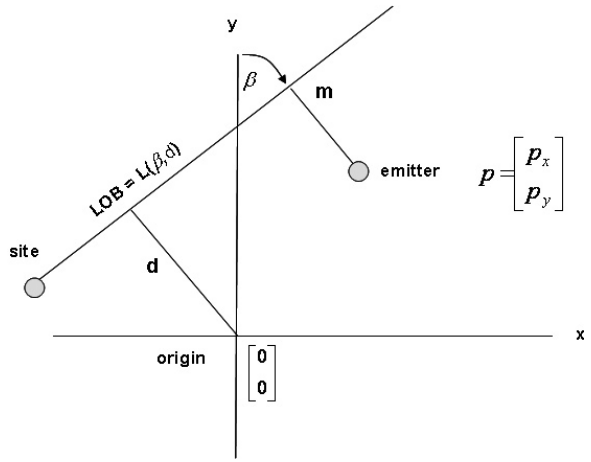

FIGURE 47-20 Stansfield geolocation geometry

The goal is to find a position $\hat{\mathbf{p}}$ that minimizes $\mathbf{m}^T\mathbf{m} = \Sigma_1^K m_i^2$, which can be done in an iterative approach using the gradient form of Eq. 47-47, The iterative improvement in position is

$$d\mathbf{p} = \text{inv}(\mathbf{A}^T\mathbf{A}) \cdot (\mathbf{A}^T\mathbf{m}) \tag{47-48}$$

and

$$\hat{\mathbf{p}}_{\text{new}} = \hat{\mathbf{p}}_{\text{old}} + d\mathbf{p} \tag{47-49}$$

Inspection of the components of Eq. 47-48 reveals that the $\mathbf{A}^T\mathbf{A}$ and $\mathbf{A}^T\mathbf{m}$ matrices are the classic unweighted least squares normal equations. These should be used on the first iteration from an arbitrary starting point $\mathbf{p}_o$. Subsequent iterations should use a weighted version of $\mathbf{A}^T\mathbf{A}$ and $\mathbf{A}^T\mathbf{m}$ that account for the LOB a priori DF variance σ^2_{LOB} and distance r_i from the ith bearing site to emitter. Using a covariance matrix $\mathbf{R}$ whose diagonal elements contain the squared weights $w_i^2 = 1/(\sigma^2_{\text{LOB}} r_i^2)$, Eq. 47-48 is modified to be

$$d\mathbf{p} = \text{inv}(\mathbf{A}^T\mathbf{R}\mathbf{A}) \cdot (\mathbf{A}^T\mathbf{R}\mathbf{m}) \tag{47-50}$$

The weighted normal equations are written as

$$(\mathbf{A}^T\mathbf{R}\mathbf{A}) = \begin{bmatrix} \sum_{i=1}^{K} \frac{\cos^2(\beta_i)}{\sigma^2_{\text{LOB}} r_i^2} & -\sum_{i=1}^{K} \frac{\cos(\beta_i)\sin(\beta_i)}{\sigma^2_{\text{LOB}} r_i^2} \\ -\sum_{i=1}^{K} \frac{\cos(\beta_i)\sin(\beta_i)}{\sigma^2_{\text{LOB}} r_i^2} & \sum_{i=1}^{K} \frac{\sin^2(\beta_i)}{\sigma^2_{\text{LOB}} r_i^2} \end{bmatrix} \tag{47-51}$$

TABLE 47-2 Ellipse Confidence Factor

Ellipse Confidence Factor	Scaling Factor (*jo*)
68%	1
80%	1.79
90%	2.15
95%	2.45

and

$$(\mathbf{A}^T\mathbf{Rm}) = \begin{bmatrix} -\sum_{i=1}^{K} \dfrac{m_i \cos(\beta_i)}{\sigma_{\text{LOB}}^2 r_i^2} \\ \sum_{i=1}^{K} \dfrac{m_i \sin(\beta_i)}{\sigma_{\text{LOB}}^2 r_i^2} \end{bmatrix} \tag{47-52}$$

Convergence to $\hat{\mathbf{p}}$ requires only three or four iterations from an arbitrary starting point, making the Stansfield geolocation algorithm fairly efficient. It is customary to estimate a confidence containment ellipse about the location $\hat{\mathbf{p}}$, which can be determined from the eigenvalues of the $inv(\mathbf{A}^T\mathbf{RA})$ matrix. Letting the inverse matrix be noted as $\mathbf{Q}$, the eigenvalues are found by solving the determinate $|\lambda\mathbf{I} - \mathbf{Q}| = 0$. Two eigenvalues result, designated λ_+ (maximum) and λ_- (minimum). The confidence ellipse is scaled by the number of LOBs, K, and by a scaling factor, *jo*, which establishes the statistical confidence level (see Table 47-2).

The confidence ellipse is then described by the semi-major and semi-minor axes:

$$s\,\text{maj} = jo\lambda_+\sqrt{\frac{K}{K-1}} \text{ and } s\,\text{min} = jo\lambda_-\sqrt{\frac{K}{K-1}} \tag{47-53}$$

The unambiguous ellipse orientation (see Table 47-3) requires testing of the terms of the $\mathbf{Q}$ matrix.

A Monte Carlo simulation of LOBs from three bearing sites illustrates the Stansfield algorithm. LOBs with 2° rms error were generated from three sites, producing a best estimate position and 95 percent confidence containment ellipse (see Figure 47-21*a*). To evaluate 300 trials, the confidence ellipse, normally centered on each estimated position, is shifted to the true emitter location, and allows comparison of the theoretical 68%, 80%, and 95% confidence ellipse containment with the trial estimated positions (see Figure 47-21*b*).

TABLE 47-3 Confidence Ellipse Orientation

Compare Diagonal Terms	Orientation
$Q_{1,1} <= Q_{2,2}$	$90 - \frac{1}{2}\text{atan}\,2\left(\frac{y\text{ term}}{x\text{ term}}\right)$
$Q_{1,1} > Q_{2,2}$	$\frac{1}{2}\text{atan}\,2\left(\frac{y\text{ term}}{x\text{ term}}\right)$
where	$y\text{ term} = \mathbf{Q}_{1,2} + \mathbf{Q}_{2,1}$ $x\text{ term} = \mathbf{Q}_{1,1} - \mathbf{Q}_{2,2}$

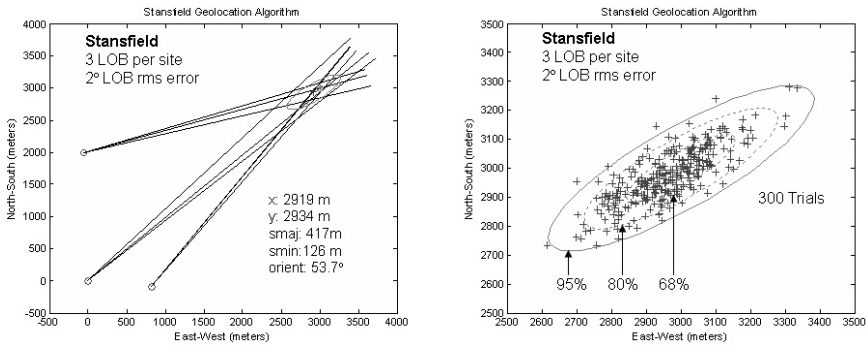

FIGURE 47-21 (*a*) Stansfield LOBs, geolocation, and 95% confidence ellipse and (*b*) 300 trials with 68%, 80%, and 95% confidence ellipse centered on the true emitter

Wangsness AOA Geolocation Algorithm

In 1973 Dennis Wangsness proposed an elegant solution to geolocation on a spherical earth.[38] It has the advantage of being a fast, non-iterative eigenvector approach to produce both geolocation and a confidence containment ellipse. Extending the spherical solution onto a geoid allows the algorithm to be WGS-84 compliant.

Wangsness recognized that any LOB describes a great circle around the earth and is anchored through the bearing site. These great circles are described by perpendicular normal vectors, **n**, which collectively produce an eigenvector solution for best estimate of position and error ellipse.

First, the LOB normal vectors are described in terms of the Earth Centered Earth Fixed (ECEF) coordinate system and are collected into transformation matrix **A** for *K* LOBs:

$$\mathbf{A} = \begin{bmatrix} nx_1 & ny_1 & nz_1 \\ \vdots & \vdots & \vdots \\ nx_K & ny_K & nz_K \end{bmatrix} = \begin{bmatrix} \mathbf{n_1} & \cdots & \mathbf{n_i} & \cdots & \mathbf{n_K} \end{bmatrix}^T \tag{47-54}$$

where $\mathbf{n}_i = \begin{bmatrix} nx_i \\ ny_i \\ nz_i \end{bmatrix}$ is the *i*th LOB normal vector in ECEF coordinates.

Once the $\mathbf{A}^T\mathbf{A}$ matrix is formed, the Wangsness algorithm solves for the three eigenvalues and associated eigenvectors using $|\lambda\mathbf{I} - \mathbf{A}^T\mathbf{A}| = 0$. The normalized eigenvector associated with the smallest eigenvalue is a unit vector that points toward the best estimate of emitter position. This unit vector can be transformed into spherical latitude and longitude and further transformed into geodetic latitude and longitude using a standard geoid such as WGS-84.

Although the eigen solution is not iterative, once an approximate emitter position is found, a weighted solution using the covariance error matrix $\mathbf{R} = \text{diag}(1/r_i^2)$, where r_i is the arc distance between the *i*th-LOB bearing site and the estimated location. The $\mathbf{A}^T\mathbf{A}$ matrix now becomes the weighted matrix $\mathbf{A}^T\mathbf{R}\mathbf{A}$.

The three eigenvalues of $|\lambda \mathbf{I} - \mathbf{A}^T\mathbf{R}\mathbf{A}| = 0$ are sorted smallest to largest (λ_1, λ_2, and λ_3) to provide the confidence ellipse equations:

$$s\ \text{maj} = \frac{a_e \cdot jo}{\sqrt{K-2}} \cdot \sqrt{\frac{\lambda_1}{\lambda_2}} \quad \text{and} \quad s\ \text{min} = \frac{a_e \cdot jo}{\sqrt{K-2}} \cdot \sqrt{\frac{\lambda_1}{\lambda_3}} \tag{47-55}$$

where K is the number of LOBs, jo is the ellipse scaling factor for confidence of containment, and a_e is the earth's radius to convert arc distances into meters. Ellipse orientation is derived from the arc cosine of the dot product formed by the eigenvector associated with λ_2 (the eigenvalue associated with semi-major axis) and a unit vector at the estimated location that points east.

A similar Monte Carlo simulation was run for the Wangsness algorithm with the same LOB error and site geometry of the Stansfield simulation. LOB, best position, and confidence ellipse were computed (see Figure 47-22*a*) and 300 trials were made (see Figure 47-22*b*). Again, the confidence ellipse was shifted to the true emitter location, for comparison of the theoretical 68%, 80%, and 95% confidence containment ellipses.

TDOA Geolocation Algorithm

When the LORAN hyperbolic location system was first developed by MIT in 1942, it was computationally intensive and highly classified.[39] Now TDOA geolocation can be done with small radio tuners and inexpensive computer chips. The algorithm presented here is consistent with the two-dimensional Stansfield approach, but can be easily extended to a three-dimensional solution on a spherical earth or WGS-84 geoid.[40,41]

The time difference of a signal arriving at two sites $\mathbf{s}_1$ and $\mathbf{s}_2$ from an emitter at $\mathbf{s}_o$ can be written in terms of the two distances D_1 and D_2 between the sites and emitter, scaled by the speed of light, c:

$$\text{TDOA}_{ik} = \frac{D_i - D_k}{c} \tag{47-56}$$

where D_i is the distance between site $\mathbf{s}_i$ and emitter at $\mathbf{s}_o$

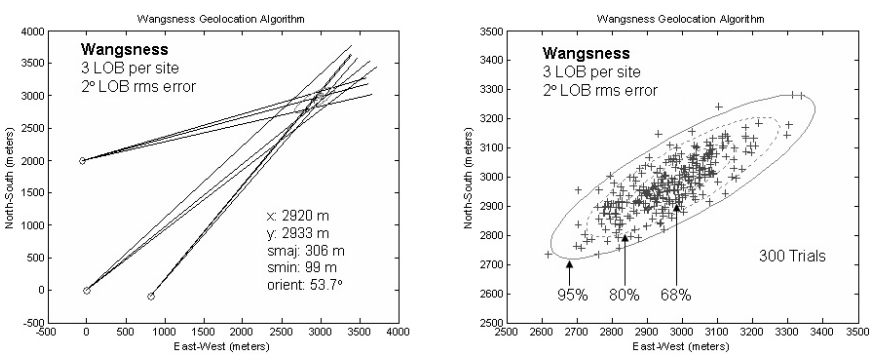

FIGURE 47-22 (*a*) Wangsness LOBs, geolocation, and 95% confidence ellipse and (*b*) 300 trials with 68%, 80%, and 95% confidence ellipse centered on the true emitter

$$D_i = |\mathbf{s}_i - \mathbf{s}_o| = \{(x_i - x_o)^2 + (y_i - y_o)^2\}^{\frac{1}{2}} \tag{47-57}$$

The hyperbolic TDOA solution of location is written in an iterative, gradient form similar to the Stansfield approach of Eqs. 47-48 and 47-49:

$$d\mathbf{s}_o = (\mathbf{A}^T\mathbf{A}) \cdot d(\mathbf{TDOA}) \tag{47-58}$$

and

$$\hat{\mathbf{s}}_{\text{new}} = \hat{\mathbf{s}}_o + d\mathbf{s}_o \tag{47-59}$$

The matrix $d(\mathbf{TDOA})$ is a $K \times 1$ vector of K observed minus calculated TDOA values from the i-k site pair, where the calculated TDOA_{ik} and its derivative are based on the current estimate of emitter position $\hat{\mathbf{s}}_o$. The $\mathbf{A}^T\mathbf{A}$ matrix is a $K \times 2$ transformation matrix of partial derivatives of TDOA_{ik} with respect to $\hat{\mathbf{s}}_o$. The fundamental $d(\mathbf{TDOA})$ vector and $\mathbf{A}$ matrix are written as

$$d(\mathbf{TDOA}) = \begin{bmatrix} \text{TDOA}_{ik}(\text{measured})_1 - \text{TDOA}_{ik}(\text{calculated})_1 \\ \text{TDOA}_{ik}(\text{measured})_2 - \text{TDOA}_{ik}(\text{calculated})_2 \\ \vdots \\ \text{TDOA}_{ik}(\text{measured})_K - \text{TDOA}_{ik}(\text{calculated})_K \end{bmatrix} \tag{47-60}$$

and

$$\mathbf{A} = \begin{bmatrix} \left\{\dfrac{\partial \text{TDOA}_{ik}}{\partial x_o} dx_o\right\}_1 & \left\{\dfrac{\partial \text{TDOA}_{ik}}{\partial y_o} dy_o\right\}_1 \\ \left\{\dfrac{\partial \text{TDOA}_{ik}}{\partial x_o} dx_o\right\}_2 & \left\{\dfrac{\partial \text{TDOA}_{ik}}{\partial y_o} dy_o\right\}_2 \\ \vdots & \vdots \\ \left\{\dfrac{\partial \text{TDOA}_{ik}}{\partial x_o} dx_o\right\}_K & \left\{\dfrac{\partial \text{TDOA}_{ik}}{\partial y_o} dy_o\right\}_K \end{bmatrix} \tag{47-61}$$

The partial differential of TDOA_{ik} with respect to the current estimate of emitter position is further expanded using the definitions of time delay from Eqs. 47-56 and 47-57:

$$\frac{\partial \text{TDOA}_{ik}}{\partial x_o} = \frac{1}{c}\left(\frac{\partial D_i}{\partial x_o} - \frac{\partial D_k}{\partial x_o}\right) = \frac{1}{c}\left(\frac{(x_o - x_i)}{D_i} - \frac{(x_o - x_k)}{D_k}\right) \tag{47-62}$$

and

$$\frac{\partial \text{TDOA}_{ik}}{\partial y_o} = \frac{1}{c}\left(\frac{\partial D_i}{\partial y_o} - \frac{\partial D_k}{\partial y_o}\right) = \frac{1}{c}\left(\frac{(y_o - y_i)}{D_i} - \frac{(y_o - y_k)}{D_k}\right) \tag{47-63}$$

At least two different site pairs are required for geolocation convergence, and care must be taken to avoid ambiguities, since, unlike LOB observations, the hyperbolic TDOA isochrones have left-right symmetry about a line between the measuring i-k site pair.

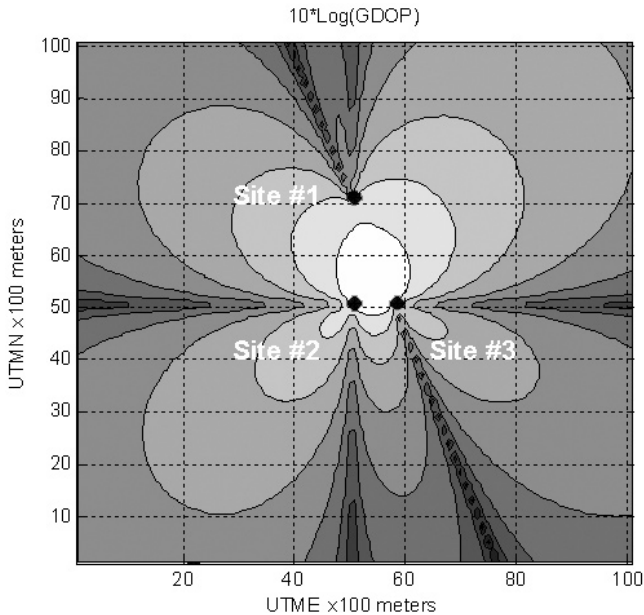

FIGURE 47-23 GDOP for TDOA geolocation from three sites. Lightest color indicates lowest GDOP and area of best geolocation.

A useful concept in evaluating the geolocation geometry is a quantity called the Geometric Dilution of Precision (GDOP), defined as

$$\text{GDOP} = \text{trace}(\text{inv}(\mathbf{A}^T\mathbf{A})) \tag{47-64}$$

A low value of GDOP indicates good geometry for the geolocation solution, while a high GDOP indicates poor geometry (see Figure 47-23).

A Monte Carlo simulation with a geometry similar to Stansfield and Wangsness was run for TDOA geolocation (see Figure 47-24). Each TDOA has $\sigma_{\text{TDOA}} = 50$-ns rms error.

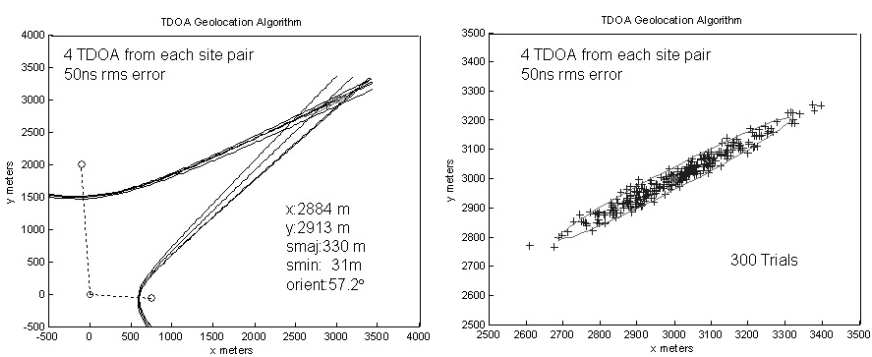

FIGURE 47-24 (*a*) TDOA hyperbolic isochrones, geolocation, and 95% confidence ellipse and (*b*) 300 trials with 95% confidence ellipse centered on the true emitter

Although the TDOA algorithm estimates position entirely in the time domain, the simulation also drew hyperbolic isochrones for comparison with the LOB geolocation approach (compare Figure 47-24*a* with Figures 47-21*a* and 47-22*b*). Four TDOA measures were made from each site pair (shown as dotted lines connecting the sites). The calculation of the confidence error ellipse closely parallels that of the Stansfield algorithm described by Eq. 47-53 and Table 47-3. In Figure 47-24*b*, the confidence ellipse is shifted to the true emitter location to examine the 95% containment of 300 geolocation trials. The TDOA geolocation error is distributed very differently from the LOB geolocation error (compare Figure 47-24*b* with Figures 47-21*b* and 47-22*b*).

REFERENCES

1. F.E. Terman, *Radio Engineering* (New York: McGraw-Hill, 1947): 817.
2. National Telecommunications and Information Administration (NITA), *Manual of Regulations and Procedures for Federal Radio Frequency Management*, Section 6.1.1 (Jan. 1993): 6–12.
3. F. B. Gross, *Smart Antennas for Wireless Communications with MatLab* (New York: McGraw-Hill, 2005).
4. S. C. Hooper, "Navy History—Radio, Radar, and Sonar," Recordings, Office of Naval History, Washington, D.C., 31R76. [Quoted references may be found in L. S. Howeth, *History of Communications-Electronics in the United States Navy*, Chapter XII, "The Radio Direction Finder": http://earlyradiohistory.us/1963hw22.htm.]
5. L. S. Howeth, *History of Communications-Electronics in the United States Navy* (Washington, D.C.: United States Government Printing Office, 1963): http://earlyradiohistory.us/1963hw.htm.
6. F. H. Engel and F. W. Dunmore, "A Directive Type of Radio Beacon and Its Application to Navigation," *Scientific Papers Bureau of Standards*, vol. 19 (1923): 281–295.
7. G. Spinger, "Radio Systems in the Early A6M Zero," http://www.jaircraft.com/research/gregspringer/radios/radio_systems.htm.
8. "History or Radio Research at Ditton Park," http://www.dittonpark-archive.rl.ac.uk/histTime.html.
9. D. Kahn, *The Codebreakers* (New York: Macmillan Co., 1969): 8/504.
10. V.A. Kotelnikov, "Determination of the Elements of the Orbit of a Satellite Using the Doppler Effect," *Radiotechnika and Electronika*, vol. 7 (July 1958): 873–991.
11. C. Soanes, "Orbital Navigation Systems—Present and Future Systems," Dynamic Positioning Maritime Technology Society Conference, London, Sept. 28–30, 2004. [Paper available at http://dynamic-positioning.com/dp2004/sensors_soanes.pdf.]
12. P. Daly and G. E. Perry, "Recent Developments with the Soviet Union's VHF Satellite Navigation System," *Space Communications and Broadcasting*, vol. 4 (1986): 51–61.
13. F. W. Lehan and G. L. Brown, Discovery and Location System (Nov. 6, 1962): U.S. Pat. 3,063,048.
14. http://www.cospas-sarsat.org/ and http://www.sarsat.noaa.gov/.
15. R. O. Schmidt, "Multiple Emitter Location and Signal Parameter Estimation," *IEEE Trans. on Antennas and Propagation*, vol. AP-34(3) (1986): 276–280.
16. R. Roy and T. Kailath, "ESPRIT—Estimation of Signal Parameters via Rotational Invariance Techniques," *IEEE Trans. Acoustics, Speech, and Sig. Proc.*, vol. ASSP-37 (July 1989) 984–995.
17. A. Moffet, "Minimum-Redundancy Linear Arrays," *IEEE Trans AP*, vol. 16(2) (1968): 172–175.
18. S. Stein, "Algorithms for Ambiguity Function Processing," *IEEE Trans. Acoustics, Speech, and Signal Processing*, vol. ASSP-29 (June 1981): 588–599.
19. C. Knapp and G. C. Carter, "The Generalized Correlation Method for Estimation of Time Delay," *IEEE Trans. Acoustics, Speech, and Sig. Proc.*, vol. ASSP-24 (Aug. 1976).
20. P. J. D. Gething, *Radio Direction Finding and Superresolution,* 2nd Ed. (London: Peter Peregrinus Ltd. on behalf of IEE, 1991): 94–113.

21. C. W. Earp and R. M. Godfrey, "Radio Direction Finding by Measurement of the Cyclical Difference of Phase," *J. IEE (London)*, part IIIA, vol. 94 (March 1947): 705.
22. F. Adcock, Improvements in Means for Determining the Direction of a Distant Source of Electro-Magnetic Radiation (1919): British Pat. 130,490.
23. R. Poisel, *Introduction to Communication Electronic Warfare Systems* (Boston: Artech House, 2002): 352–359.
24. D. H. Johnson, "The Application of Spectral Estimation Methods to Bearing Estimation Problems," *Proc. IEEE*, vol. 70(9) (Sept. 1982): 1018–1028.
25. J. P. Burg, "Maximum Entropy Spectrum Analysis," Ph.D. dissertation, Dept. of Geophysics, Stanford University, Stanford, CA, 1975.
26. V. F. Pisarenko, "The Retrieval of Harmonics from a Covariance Function," *Geophys. J. Royal Astronomical Soc.*, vol. 33 (1973): 347–366.
27. R. Kumaresan and D. W. Tufts, "Estimating the Angles of Arrival of Multiple Plane Waves," *IEEE Trans. Aerospace Electron. Sys.*, vol. AES-19 (Jan. 1983) 134–139.
28. I. Ziskind and M. Wax, "Maximum Likelihood Localization of Multiple Sources by Alternating Projection," *IEEE Trans. Acoustics, Speech, and Sig. Proc.*, vol. ASSP-36 (Oct. 1988): 1553–1560.
29. E. Anderson et al, *LAPACK Linear Algebra Package*, http://math.nist.gov/lapack++/.
30. J. Volder, "The CORDIC Computing Technique," *IRE Trans. Computers*, vol. EC-8 (Sept. 1959): 330–334.
31. A. Ahmedsaid, A. Amira, and A. Bouridane, "Improved SVD Systolic Array and Implementation on FPGA," *Proc. 2003 IEEE Inter. Conf. on Field-Programmable Technology (FPT)* (Dec. 15–17, 2003): 35–42.
32. G. W. Stewart, *Matrix Algorithms Vol. II: Eigensystems* (Philadelphia: Society for Industrial and Applied Mathematics, 2001): 56–70.
33. H.L. Van Trees, *Optimum Array Processing* (New York: Wiley Interscience, 2002): 925–932.
34. H.L. Van Trees, *Optimum Array Processing*: 827–845.
35. H. Akaike, "A New Look at the Statistical Model Identification," *IEEE Trans. Automatic Control*, vol. AC-19 (June 1974): 716–723.
36. M. Wax and T. Kailath, "Detection of Signals by Information Theoretic Criteria," *IEEE Trans. Acoustics, Speech, and Sig. Proc.*, vol. ASSP-33 (April 1985): 387–392.
37. R. G. Stansfield, "Statistical Theory of DF Fixing," *J. IEE (London)*, part IIIA, vol. 94 (1947): 762–770.
38. D. Wangsness, "A New Method of Position Estimation Using Bearing Measurements," *IEEE Trans. Aerospace and Electronic Sys.* (Nov. 1973): 959–960.
39. D. A. Grier, *When Computers Were Human* (Princeton, NJ: Princeton University Press, 2005): 249–250.
40. A. D. Stewart, "Comparing Time-Based and Hybrid Time-Based/Frequency Based Multi-Platform Geolocation Systems," Thesis, Naval Postgraduate School, Monterey, CA, Sept. 1997.
41. H. C. Schau and A. Z. Robinson, "Passive Source Location Employing Spherical Surfaces from Time-of-Arrival Differences," *IEEE Trans. Acoustics, Speech, and Sig. Proc*., vol. ASSP-35 (Aug. 1987) 1223–1225.